AD-A247 338

Quarterly Technical Report

Solid State Research

DTIC
ELECTE
MAR 0 9 1992
S B D

1991:3

| Lincoln Laboratory | |
| --- | --- |
| MASSACHUSETTS INSTITUTE OF TECHNOLOGY | |
| LEXINGTON, MASSACHUSETTS | |

92-05870

92 3 04 077

This technical report has been reviewed and is approved for publication.

FOR THE COMMANDER
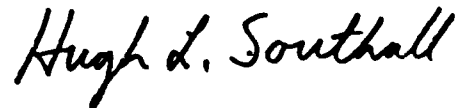
*Hugh L. Southall*

Hugh L. Southall, Lt. Col., USAF
Chief, ESD Lincoln Laboratory Project Office

MASSACHUSETTS INSTITUTE OF TECHNOLOGY
LINCOLN LABORATORY

# SOLID STATE RESEARCH

## QUARTERLY TECHNICAL REPORT

1 MAY — 31 JULY 1991

ISSUED 16 DECEMBER 1991

LEXINGTON                                    MASSACHUSETTS

# ABSTRACT

This report covers in detail the research work of the Solid State Division at Lincoln Laboratory for the period 1 May through 31 July 1991. The topics covered are Electrooptical Devices, Quantum Electronics, Materials Research, Submicrometer Technology, High Speed Electronics, Microelectronics, and Analog Device Technology. Funding is provided primarily by the Air Force, with additional support provided by the Army, DARPA, Navy, SDIO, NASA, and DOE.

DTIC
COPY
INSPECTED
6

| Accession For | |
|---|---|
| NTIS GRA&I | ☑ |
| DTIC TAB | ☐ |
| Unannounced | ☐ |
| Justification | |

By_____

Distribution/

Availability Codes

| Dist | Avail and/or Special |
|---|---|
| A-1 | |

iii

# TABLE OF CONTENTS

# TABLE OF CONTENTS (Continued)

# LIST OF ILLUSTRATIONS

# LIST OF ILLUSTRATIONS (Continued)

# INTRODUCTION

## 1. ELECTROOPTICAL DEVICES

A Y-junction interferometer phase measurement technique has been developed that is independent of the power or power ratio in the input arms. This technique was incorporated into an AlGaAs guided-wave Mach-Zehnder interferometer to demonstrate phase measurement and correction of set phase differences at power imbalances of up to 15% between the interferometer arms.

A model has been developed for mass transport of two-dimensional surface profiles for which a Cartesian coordinate system can be conveniently used. Simple analytical solutions have been obtained that provide valuable insights for the fabrication of microoptical structures.

## 2. QUANTUM ELECTRONICS

A mode of laser operation has been discovered that allows a single Nd:YAG laser with an intracavity nonlinear crystal to stably generate light at the 589-nm sum frequency of the 1064- and 1320-nm outputs. The dynamics of this new mode of operation has been investigated experimentally.

The frequency response of the microchip laser to pump-power modulation has been derived in closed form. It is shown that pump-power modulation is a viable technique to change the output frequency of microchip lasers.

## 3. MATERIALS RESEARCH

Strained InGaAs/AlGaAs quantum-well diode lasers have been fabricated on Si substrates for the first time, with the objective of improving laser reliability by incorporating In in the active layer to inhibit the propagation of dark-line defects. One graded-index separate-confinement heterostructure single-quantum-well laser with an $In_{0.05}Ga_{0.95}As$ active layer has operated CW for 56.5 h, a record lifetime for GaAs-based diode lasers on Si.

## 4. SUBMICROMETER TECHNOLOGY

Thin films of polysilyne have been patterned by exposure with 193-nm radiation followed by selective etching of the unexposed areas in a HBr plasma. Patterns with 0.2-$\mu$m resolution and high aspect ratio were obtained when this dry development process was applied to bilayers consisting of polysilyne on an organic planarizing layer.

Cold cathodes have been produced in semiconducting $p$-type diamond by fabricating mesa-etched diodes. When forward biased, the diodes emit current into vacuum with efficiencies up to $2 \times 10^{-4}$, which can be further enhanced in the presence of $O_2$.

# 5. HIGH SPEED ELECTRONICS

A $CO_2$ laser modulator has been demonstrated that utilizes the intersubband transitions of cross-gap-generated electrons in a GaAs/AlGaAs multiple-quantum-well structure. With the use of only 100 mW of cross-gap pump power in this optically controlled device, 90% modulation of the transmitted beam from a 0.5-W $CO_2$ laser has been achieved.

# 6. MICROELECTRONICS

Charge-transfer inefficiency (CTI) as a function of temperature from 100 to 220 K has been measured in buried-channel charge-coupled device (CCD) imagers made on wafers from various sources. The results show that the CTI varies significantly depending on the silicon wafer source and that for the best material it remains $< 10^{-4}$ down to 120 K.

# 7. ANALOG DEVICE TECHNOLOGY

Focal plane arrays for operation at temperatures down to 50 K have been fabricated utilizing a two-step buried-channel CCD structure. Very satisfactory performance has been demonstrated, in good agreement with the simulations.

A matched pair of high-$T_c$ superconductive chirp filters has been used to generate a compressed pulse at 77 K. These chirp filters were fabricated from thin films of $YBa_2Cu_3O_{7-x}$ on 50-cm-diam. $LaAlO_3$ substrates and have a bandwidth of 2.7 GHz, a dispersive delay of 11 ns, and a total delay of 14 ns, including the tapered-line impedance transformers.

# REPORTS ON SOLID STATE RESEARCH

## 1 May Through 31 July 1991

### PUBLICATIONS

| | | |
|---|---|---|
| Laser Deposition and Etching of Three-Dimensional Microstructures | T. M. Bloomstein D. J. Ehrlich | *1991 Int. Conf. Solid-State Sensors and Actuators Tech. Dig.* (IEEE, New York, 1991), p. 507 |
| Reduced-Confinement GaAlAs Tapered Waveguide Antennas for Enhanced Far-Field Beam Directionality | D. E. Bossi W. D. Goodhue L. M. Johnson R. H. Rediker | *IEEE J. Quantum Electron.* **27**, 687 (1991) |
| An Abuttable CCD Imager for Visible and X-Ray Focal Plane Arrays | B. E. Burke R. W. Mountain D. C. Harrison M. W. Bautz* J. P. Doty* G. R. Ricker* P. J. Daniels | *IEEE Trans. Electron Devices* **38**, 1069 (1991) |
| Ultraviolet, Visible, and Infrared Response of PtSi Schottky-Barrier Detectors Operated in the Front-Illuminated Mode | C. K. Chen B. A. Nechay B-Y. Tsaur | *IEEE Trans. Electron Devices* **38**, 1094 (1991) |
| High-Power-Density GaAs MISFET's with a Low-Temperature-Grown Epitaxial Layer as the Insulator | C. L. Chen F. W. Smith B. J. Clifton L. J. Mahoney M. J. Manfra A. R. Calawa | *IEEE Electron Device Lett.* **12**, 306 (1991) |
| MBE Growth of GaInAsSb/AlGaAsSb Double Heterostructures for Infrared Diode Lasers | S. J. Eglash H. K. Choi G. W. Turner | *J. Cryst. Growth* **111**, 669 (1991) |
| MBE Growth of GaInAsSb/AlGaAsSb Double Heterostructures for Diode Lasers Emitting Beyond 2 $\mu$m | S. J. Eglash H. K. Choi G. W. Turner M. C. Finn | *Proc. Mater. Res. Soc. Symp.* **216**, 207 (1991) |

* Author not at Lincoln Laboratory.

| | | |
|---|---|---|
| Fast Room-Temperature Growth of SiO$_2$ Films by Molecular-Layer Dosing | D. J. Ehrlich J. Melngailis | *Appl. Phys. Lett.* **58**, 2675 (1991) |
| Diamond Transistor Performance and Fabrication | M. W. Geis | *Proc. IEEE* **79**, 669 (1991) |
| Large-Area Mosaic Diamond Films Approaching Single-Crystal Quality | M. W. Geis H. I. Smith* A. Argoitia* J. Angus* G.-H. M. Ma* J. T. Glass* J. Butler* C. J. Robinson* R. Pryor* | *Appl. Phys. Lett.* **58**, 2485 (1991) |
| Evaluation of Phenolic Resists for 193-nm Surface Imaging | M. A. Hartney D. W. Johnson* A. C. Spencer* | *Proc. SPIE* **1466**, 238 (1991) |
| Positive-Tone Silylation Processes at 193 nm | M. A. Hartney M. Rothschild R. R. Kunz D. J. Ehrlich D. C. Shaver | *Microelectron. Eng.* **13**, 51 (1991) |
| Silylation Using Focused Ion Beam Exposed Resists | M. A. Hartney D. C. Shaver M. I. Shepard* J. S. Huh* J. Melngailis* | *Appl. Phys. Lett.* **59**, 485 (1991) |
| Polysilyne Resists for 193-nm Excimer Laser Lithography | R. R. Kunz P. A. Bianconi* M. W. Horn R. R. Paladugu D. C. Shaver D. A. Smith* C. A. Freed* | *Proc. SPIE* **1466**, 218 (1991) |
| Photoreactions in Polyalkylsilynes Induced by ArF-Laser Irradiation | R. R. Kunz P. A. Bianconi* M. W. Horn D. A. Smith* C. A. Freed* | *Proc. Mater. Res. Soc. Symp.* **204**, 501 (1991) |

* Author not at Lincoln Laboratory.

| | | |
|---|---|---|
| Room-Temperature Diode-Pumped Yb:YAG Laser | P. Lacovara<br>H. K. Choi<br>C. A. Wang<br>R. L. Aggarwal<br>T. Y. Fan | *Opt. Lett.* **16**, 1089 (1991) |
| Ultrafast, Room-Temperature, Resonance-Enhanced Third-Order Optical Susceptibility Tensor of an AlGaAs/GaAs Quantum Well | H. Q. Le<br>S. DiCecca | *Opt. Lett.* **16**, 901 (1991) |
| Scalable High-Power Optically Pumped GaAs Laser | H. Q. Le<br>S. DiCecca<br>A. Mooradian | *Appl. Phys. Lett.* **58**, 1967 (1991) |
| High-Temperature Superconductive Passive Microwave Devices | W. G. Lyons<br>R. S. Withers<br>J. M. Hamm<br>A. C. Anderson<br>P. M. Mankiewich*<br>M. L. O'Malley*<br>R. E. Howard*<br>R. R. Bonetti*<br>A. E. Williams*<br>N. Newman* | *1991 IEEE MTT-S Int. Microwave Symp. Dig.* (IEEE, New York, 1991), Vol. 3, p. 1227 |
| Stripline Resonators for Characterization of High-$T_c$ Superconducting Films for Device Applications | D. E. Oates<br>A. C. Anderson<br>P. M. Mankiewich* | *Science and Technology of Thin Film Superconductors 2,* R. D. McConnell and R. Noufi, eds. (Plenum, New York, 1990), p. 579 |
| Optical Transmitter for Fiber Optic Interconnects | P. R. Prucnal*<br>S. D. Elby*<br>K. B. Nichols | *Opt. Eng.* **30**, 511 (1991) |
| Operation of a Coherent Ensemble of Five Diode Lasers in an External Cavity | R. H. Rediker<br>K. A. Rauschenbach<br>R. P. Schloss | *IEEE J. Quantum Electron.* **27**, 1582 (1991) |
| Liquid-Nitrogen-Cooled Ti:Al$_2$O$_3$ Lasers | P. A. Schulz<br>S. R. Henion | *IEEE J. Quantum Electron.* **27**, 1039 (1991) |

---

* Author not at Lincoln Laboratory.

| | | |
|---|---|---|
| Current Distribution, Resistance, and Inductance for Superconducting Strip Transmission Lines | D. M. Sheen*<br>S. M. Ali*<br>D. E. Oates<br>R. S. Withers<br>J. A. Kong* | *IEEE Trans. Appl. Superconduct.*<br>**1**, 108 (1991) |
| Current Distribution in Superconducting Strip Transmission Lines | D. M. Sheen*<br>S. M. Ali*<br>D. E. Oates<br>R. S. Withers<br>J. A. Kong* | *1991 IEEE MTT-S Int.*<br>*Microwave Symp. Dig.*<br>(IEEE, New York, 1991),<br>Vol. 1, p. 161 |
| A 1.57 W/mm GaAs-Based MISFET for High-Power and Microwave-Switching Applications | F. W. Smith<br>C. L. Chen<br>L. J. Mahoney<br>M. J. Manfra<br>D. H. Temme<br>B. J. Clifton<br>A. R. Calawa | *1991 IEEE MTT-S Int.*<br>*Microwave Symp. Dig.*<br>(IEEE, New York, 1991),<br>Vol. 2, p. 643 |
| High-Speed Optical Interconnections for Digital Systems | D. Z. Tsang | *Lincoln Lab. J.* **4**, 31 (1991) |
| Long-Wavelength $Ge_xSi_{1-x}$/Si Heterojunction Infrared Detectors and 400 × 400-Element Imager Arrays | B-Y. Tsaur<br>C. K. Chen<br>S. A. Marino | *IEEE Electron Device Lett.*<br>**12**, 293 (1991) |
| Application of Frequency-Domain Analysis to RHEED Oscillation Data: Time Dependence of AlGaAs Growth Rates | G. W. Turner<br>S. J. Eglash | *J. Cryst. Growth* **111**, 105 (1991) |
| Organometallic Vapor Phase Epitaxy of High-Performance Strained-Layer InGaAs–AlGaAs Diode Lasers | C. A. Wang<br>H. K. Choi | *IEEE J. Quantum Electron.*<br>**27**, 681 (1991) |
| AlInGaAs/AlGaAs Separate-Confinement Heterostructure Strained Single Quantum Well Diode Lasers Grown by Organometallic Vapor Phase Epitaxy | C. A. Wang<br>J. N. Walpole<br>L. J. Missaggia<br>J. P. Donnelly<br>H. K. Choi | *Appl. Phys. Lett.* **58**, 2208 (1991) |
| Polarization-Switchable Microchip Lasers | J. J. Zayhowski | *Appl. Phys. Lett.* **58**, 2746 (1991) |

* Author not at Lincoln Laboratory.

# ACCEPTED FOR PUBLICATION

| | | |
|---|---|---|
| Resonant Tunneling in High-Speed Double-Barrier Diodes | E. R. Brown | In *Hot Carriers in Semiconductor Microstructures*, J. Shah, ed. (Academic, Orlando, Fla.) |
| GaAs/AlGaAs Dynamic Random Access Memory Cell | C. L. Chen<br>W. D. Goodhue<br>L. J. Mahoney | *Electron. Lett.* |
| 375-GHz-Bandwidth Metal-Semiconductor-Metal Photoconductive Detector | Y. Chen*<br>S. Williamson*<br>T. Brock*<br>F. W. Smith<br>A. R. Calawa | *Appl. Phys. Lett.* |
| Room-Temperature CW Operation at 2.2 $\mu$m of GaInAsSb/AlGaAsSb Diode Lasers Grown by Molecular Beam Epitaxy | H. K. Choi<br>S. J. Eglash | *Appl. Phys. Lett.* |
| High-Power, High-Temperature Operation of Strained Single-Quantum-Well Diode Lasers | H. K. Choi<br>C. A. Wang<br>D. F. Kolesar<br>R. L. Aggarwal<br>J. N. Walpole | *IEEE Photon. Technol. Lett.* |
| Operation of Five Individual Diode Lasers as a Coherent Ensemble by Fiber Coupling into an External Cavity | C. J. Corcoran<br>R. H. Rediker | *Appl. Phys. Lett.* |
| Single-Axial Mode, Intracavity-Doubled Nd:YAG Laser | T. Y. Fan | *IEEE J. Quantum Electron.* |
| Diamond Cold Cathodes | M. W. Geis<br>N. N. Efremow<br>J. D. Woodhouse<br>M. D. McAleese<br>M. Marchywka*<br>D. G. Socker*<br>J. F. Hochedez* | *IEEE Electron Device Lett.* |

---

* Author not at Lincoln Laboratory.

| | | |
|---|---|---|
| Monolithic Two-Dimensional Surface-Emitting Strained-Layer InGaAs/AlGaAs and AlInGaAs/AlGaAs Diode Laser Arrays with over 50% Differential Quantum Efficiencies | W. D. Goodhue J. P. Donnelly C. A. Wang G. A. Lincoln K. Rauschenbach R. J. Bailey G. D. Johnson | *Appl. Phys. Lett.* |
| Subpicosecond Carrier Lifetime in GaAs Grown by Molecular Beam Epitaxy at Low Temperatures | S. Gupta* M. Y. Frankel* J. A. Valdmanis* J. F. Whitaker* G. A. Mourou* F. W. Smith A. R. Calawa | *Appl. Phys. Lett.* |
| Surface Imaging of Focused Ion Beam Exposed Resists | M. A. Hartney D. C. Shaver M. I. Sheppard* J. S. Huh* J. Melngailis V. Medvedev* | *J. Vac. Sci. Technol. B* |
| 5-GHz Mode Locking of a Nd:YLF Laser | S. R. Henion P. A. Schulz | *Opt. Lett.* |
| CW Operation of a Diode-Pumped Rotating Nd:Glass Disk Laser | J. Korn T. H. Jeys T. Y. Fan | *Opt. Lett.* |
| Optical Phase Difference Measurement and Correction Using AlGaAs Integrated Guided-Wave Components | S. D. Lau J. P. Donnelly C. A. Wang R. B. Goodman R. H. Rediker | *IEEE Photon. Technol. Lett.* |

* Author not at Lincoln Laboratory.

| | | |
|---|---|---|
| Microstructure of Annealed Low-Temperature-Grown GaAs Layers | Z. Liliental-Weber*<br>A. Calverie*<br>J. Washburn*<br>F. W. Smith<br>A. R. Calawa | *Appl. Phys. Lett.* |
| Excimer-Laser Induced Sub-0.5-μm Patterning of WO₃ Thin Films | M. Rothschild<br>A. R. Forte | *Appl. Phys. Lett.* |
| Through-Wafer Optical Communication Using Monolithic InGaAs-on-Si LEDs and Monolithic PtSi-Si Schottky-Barrier Detectors | G. W. Turner<br>C. K. Chen<br>B-Y. Tsaur<br>A. M. Waxman | *IEEE Photon. Technol. Lett.* |
| Role of GaAs Bounding Layers in Improving OMVPE Growth and Performance of Strained-Layer InGaAs/AlGaAs Single-Quantum-Well Diode Lasers | C. A. Wang<br>H. K. Choi | *J. Electron. Mater.* |
| Optimization of Q-Switched Lasers | J. J. Zayhowski<br>P. L. Kelley | *IEEE J. Quantum Electron.* |

In the "Through-Wafer" row the journal is *IEEE Photon. Technol. Lett.*; the "WO₃" chemical formula uses subscript 3.

## PRESENTATIONS[†]

| | | |
|---|---|---|
| InGaAs/AlGaAs and AlInGaAs/AlGaAs Strained Quantum-Well Diode Lasers | H. K. Choi | Seminar, Optics and Quantum Electronics,<br>Cambridge, Massachusetts,<br>1 May 1991 |
| Growth and Characterization of a High-Power GaAs-Based MISFET | F. W. Smith<br>C. L. Chen<br>M. J. Manfra<br>L. J. Mahoney<br>C. A. Graves<br>A. R. Calawa | Electrochemical Society Meeting,<br>Washington, D.C.,<br>5-10 May 1991 |

---

\* Author not at Lincoln Laboratory.

[†] Titles of presentations are listed for information only. No copies are available for distribution.

| | | |
|---|---|---|
| Nucleation and Growth Processes in Chemical Vapor Deposition of Diamond | J. C. Angus* <br> R. Gat* <br> Z. Li* <br> M. Sunkara* <br> M. W. Geis | |
| Diamond Cold Cathodes | M. W. Geis <br> N. N. Efremow <br> J. D. Woodhouse <br> M. D. McAleese | Second International Symposium on Diamond Materials, Washington, D.C., 5-10 May 1991 |
| Production of Large-Area Mosaic Diamond Films Approaching Single-Crystal Quality | M. W. Geis <br> H. I. Smith* | |
| Interferometric Modulators for Bandpass Analog Optical Systems | L. M. Johnson <br> H. V. Roussell | Workshop on Integrated Optics for Military Applications, Huntsville, Alabama, 7-9 May 1991 |
| High-Power AlInGaAs/AlGaAs Strained Single Quantum-Well Diode Lasers | H. K. Choi <br> C. A. Wang <br> R. Aggarwal <br> J. N. Walpole | |
| GaAs/AlGaAs Diode Lasers Fabricated on Substrates Prepared by Selective Growth of GaAs on Si Wafers | H. K. Choi <br> C. A. Wang <br> N. H. Karam* | |
| Scalable Optically Pumped External Cavity GaAs Lasers | S. DiCecca <br> H. Q. Le <br> A. Mooradian | 1991 Conference on Lasers and Electro-Optics, Baltimore, Maryland, 12-17 May 1991 |
| Integrated-Optical Modulators for Analog Optical Systems | L. M. Johnson <br> G. E. Betts | |
| Relative Frequency Locking of 1.32-$\mu$m Microchip Lasers Using Pump-Diode Modulation | J. A. Keszenheimer* <br> J. J. Zayhowski | |
| CW Operation of a Diode-Pumped Rotating Nd:Glass Disk Laser | J. Korn <br> T. H. Jeys <br> T. Y. Fan | |

* Author not at Lincoln Laboratory.

| | | |
|---|---|---|
| Room-Temperature InGaAs Diode-Pumped Yb:YAG Laser | P. Lacovara<br>C. A. Wang<br>H. K. Choi<br>R. L. Aggarwal<br>T. Y. Fan | 1991 Conference on Lasers and Electro-Optics, Baltimore, Maryland, 12-17 May 1991 |
| Polarization Switching of Microchip Lasers | J. J. Zayhowski | |
| Ultrafast Optical Switching via Nondegenerate Four-Wave Mixing in Waveguides | H. Q. Le | 1991 International Quantum Electronics Conference. Baltimore, Maryland, 12-17 May 1991 |
| Microchip Lasers | J. J. Zayhowski | |
| Surface Imaging of Focused Ion Beam Exposed Resists | M. A. Hartney<br>D. C. Shaver<br>M. I. Sheppard*<br>J. S. Huh*<br>J. Melngailis<br>V. Medvedev* | 35th International Symposium on Electron, Ion, and Photon Beams, Seattle, Washington, 28-31 May 1991 |
| Sub-0.25-$\mu$m Lithography at 193 nm Using HBr Dry Development of Organosilicon Resists | M. W. Horn<br>R. R. Kunz<br>R. R. Paladugu | |
| Superconducting Thin-Film $YBa_2Cu_3O_{7-x}$ Resonators and Filters | D. E. Oates<br>W. G. Lyons<br>A. C. Anderson | 45th Annual Symposium on Frequency Control, Los Angeles, California, 29-31 May 1991 |
| Future Development for Thinned, Back-Illuminated CCD Imagers | C. M. Huang | IEEE Charge-Coupled Devices Workshop, Kitchener, Ontario, Canada, 7-9 June 1991 |
| Optical Lithography at Feature Sizes of 0.25 $\mu$m and Below | D. C. Shaver | Meeting of the New England Combined Chapter, American Vacuum Society, Burlington, Massachusetts, 10 June 1991 |

* Author not at Lincoln Laboratory.

| | | |
|---|---|---|
| Quasioptical Locking of a Millimeter-Wave Resonant-Tunneling Diode Oscillator | E. R. Brown<br>C. D. Parker | |
| High-Power Properties | D. E. Oates | 1991 IEEE MTT-S<br>International Microwave<br>Symposium, |
| Stripline Resonator Measurements of $Z_s$ vs $H_{rf}$ in $YBa_2Cu_3O_{7-x}$ Thin Films | D. E. Oates<br>A. C. Anderson<br>D. M. Sheen*<br>S. M. Ali* | Boston, Massachusetts,<br>10-14 June 1991 |
| Laser-Chemical Three-Dimensional Writing of Multimaterial Structures for Microelectromechanics | T. M. Bloomstein<br>D. J. Ehrlich | Laserion '91,<br>Munich, Germany,<br>12-14 June 1991 |
| Low Shot Noise in High-Speed Resonant-Tunneling Diodes | E. R. Brown<br>C. D. Parker<br>A. R. Calawa<br>M. J. Manfra | Device Research Conference,<br>Boulder, Colorado,<br>17-19 June 1991 |
| Nb-AlO$_x$-Nb SNAP Technology for 125 mm Wafers Developed in Partnership with Silicon Technology | M. Bhushan<br>M. B. Ketchen*<br>C.-K. Hu*<br>K. Stawaisz*<br>C. Cabral*<br>M. Smyth*<br>E. Baran*<br>D. Pearson* | Fourth International Conference on Superconducting and Quantum Effect Devices and Their Applications, Berlin, Germany, 18-21 June 1991 |
| X-Ray and Photoluminescence Characterization of GaInAsP/GaAs Interfaces | S. H. Groves<br>S. C. Palmateer<br>P. A. Maki<br>D. R. Calawa | 1991 Electronic Materials Conference, Boulder, Colorado, 19-21 June 1991 |
| Microwave Applications of Superconducting Electronics | R. W. Ralston | Third International Superconductive Electronics Conference, Glasgow, Scotland, 24-28 June 1991 |
| Microwave Properties and Applications of High-$T_c$ Superconductive Thin Films | R. W. Ralston | Progress in Electromagnetics Research Symposium 1991, Cambridge, Massachusetts, 1-5 July 1991 |

* Author not at Lincoln Laboratory.

| | | |
|---|---|---|
| Frequency-Chirped Solid State Laser Radars | P. A. Schulz<br>S. R. Henion | Coherent Laser Radar:<br>Technology and<br>Applications,<br>Snowmass, Colorado,<br>8-12 July 1991 |
| Optimization of Externally Modulated Analog Optical Links for High Dynamic Range | G. E. Betts<br>L. M. Johnson<br>C. H. Cox III | |
| Nonimaging Concentrators for Diode-Pumped Slab Lasers | P. Lacovara<br>P. Gleckman*<br>R. Holman*<br>R. Winston* | SPIE's 1991 International<br>Symposium on Optical Science<br>and Engineering,<br>San Diego, California,<br>21-26 July 1991 |
| Free-Space Board-to-Board Optical Interconnections | D. Z. Tsang | |
| Long-Wavelength $Ge_xSi_{1-x}$/Si Heterojunction Infrared Detectors and Focal Plane Arrays | B-Y. Tsaur<br>C. K. Chen<br>S. A. Marino | |
| Electrical and Structural Characterization of GaAs Vertical-Sidewall Layers Grown by Atomic Layer Epitaxy | D. B. Gladden<br>C. A. Wang<br>W. D. Goodhue<br>G. A. Lincoln | |
| Fabrication of Monolithic Two-Dimensional Surface-Emitting Strained-Layer InGaAs/AlGaAs and AlInGaAs/AlGaAs Diode-Laser Arrays with over 50% Differential Quantum Efficiencies | W. D. Goodhue<br>J. P. Donnelly<br>C. A. Wang<br>G. A. Lincoln<br>R. J. Bailey<br>G. D. Johnson<br>K. Rauschenbach | IEEE Lasers and Electro-Optics Society Summer<br>Topical Meetings,<br>Newport Beach, California,<br>22 July – 2 August 1991 |
| Mass Transport Fabrication of Efficient Microlenses, Mirrors, Gratings and Monolithic Integrated Diode Lasers | Z. L. Liau | |
| Quantum Well Nonlinearities for Optical Communications | H. Q. Le | Seminar, IBM,<br>Yorktown Heights, New York,<br>26 July 1991 |
| Electronics, Optics and the Photorefractive Effect | R. C. Williamson | Topical Meeting on<br>Photorefractive Materials,<br>Effects and Devices,<br>Beverly, Massachusetts,<br>29-31 July 1991 |

* Author not at Lincoln Laboratory.

# ORGANIZATION

## SOLID STATE DIVISION

A. L. McWhorter, *Head*
I. Melngailis, *Associate Head*
E. Stern, *Associate Head*
J. F. Goodwin, *Assistant*

D. J. Ehrlich, *Senior Staff*
N. L. DeMeo, Jr., *Associate Staff*
J. W. Caunt, *Assistant Staff*
K. J. Challberg, *Administrative Staff*

## SUBMICROMETER TECHNOLOGY

D. C. Shaver, *Leader*
M. Rothschild, *Assistant Leader*

| | |
|---|---|
| Astolfi, D. K. | Goodman, R. B. |
| Craig, D. M. | Hartney, M. A. |
| Dennis, C. L. | Horn, M. W. |
| DiNatale, W. F. | Kunz, R. R. |
| Doran, S. P. | Lyszczarz, T. M. |
| Efremow, N. N., Jr. | Maki, P. A. |
| Forte, A. R. | Melngailis, J.[†] |
| Gajar, S. A.* | Sedlacek, J. H. C. |
| Geis, M. W. | Uttaro, R. S. |

## QUANTUM ELECTRONICS

A. Mooradian, *Leader*
P. L. Kelley, *Associate Leader*
A. Sanchez-Rubio, *Assistant Leader*

| | |
|---|---|
| Aggarwal, R. L. | Jeys, T. H. |
| Barch, W. E. | Korn, J. A. |
| Cook, C. C. | Lacovara, P. |
| Daneu, V. | Le, H. Q. |
| DeFeo, W. E. | Menyuk, N.[†] |
| DiCecca, S. | Nabors, C. D. |
| Dill, C. D., III | Ochoa, J. R. |
| Fan, T. Y. | Schulz, P. A. |
| Hancock, R. C. | Sullivan, D. J. |
| Henion, S. R. | Wall, K. F. |
| Hotaling, T. C. | Zayhowski, J. J. |
| Hsu, L.* | |

## ELECTRONIC MATERIALS

A. J. Strauss, *Leader*
B-Y. Tsaur, *Associate Leader*

| | |
|---|---|
| Anderson, C. H., Jr. | Kolesar, D. F. |
| Button, M. J. | Krohn, L., Jr. |
| Chen, C. K. | Marino, S. A. |
| Choi, H. K. | Mastromattei, E. L. |
| Clark, H. R., Jr. | McGilvary, W. L. |
| Connors, M. K. | Nitishin, P. M. |
| Eglash, S. J. | Pantano, J. V. |
| Fahey, R. E. | Turner, G. W. |
| Finn, M. C. | Wang, C. A. |
| Iseler, G. W. | |

## HIGH SPEED ELECTRONICS

R. A. Murphy, *Leader*
M. A. Hollis, *Assistant Leader*
R. W. Chick, *Senior Staff*

| | |
|---|---|
| Actis, R. | Manfra, M. J. |
| Barlas, A. D. | Mathews, R. H. |
| Bergeron, N. J. | Mattia, J. P.* |
| Bozler, C. O. | McIntosh, K. A. |
| Brown, E. R. | McMorran, R. A. |
| Calawa, A. R. | McNamara, M. J. |
| Chen, C. L. | Nichols, K. B. |
| Clifton, B. J. | Parker, C. D. |
| Crenshaw, D. L.* | Rabe, S. |
| Goodhue, W. D. | Rathman, D. D. |
| Gray, R. V. | Smith, F. W., III |
| Lincoln, G. A., Jr. | Vera, A. |
| Mahoney, L. J. | |

* Research Assistant
† Part Time

# 1. ELECTROOPTICAL DEVICES

## 1.1 OPTICAL PHASE DIFFERENCE MEASUREMENT AND CORRECTION USING AlGaAs INTEGRATED GUIDED-WAVE COMPONENTS

Integrated optical systems that produce a flat-phase output wavefront, independent of phase and power variations along the input wavefront, have been proposed [1],[2]. Applications include the removal of distortions produced by atmospheric turbulence from an optical wavefront and the production of a flat-phase output wavefront from an array of frequency-locked lasers. The proposed basic module of a system for use at GaAs wavelengths [2] that incorporates the phase difference measurement and correction in the same integrated optical circuit is shown in Figure 1-1. The input wavefront is coupled into straight-through waveguides via integrated optical antennas that have been developed for efficient input and output coupling, as reported previously [3]. Power from the adjacent guides is evanescently coupled to an interferometer to measure the phase difference. Feedback electronic circuits then calculate the appropriate correction voltages, which are applied to control the phase modulators on the straight-through waveguides. Because a complete integrated optical system would require an array of many such modules, phase measurement and correction must be fabrication tolerant and independent of power variations in the input wavefront. The implementation of a phase measurement and correction loop that satisfies these conditions is described here.
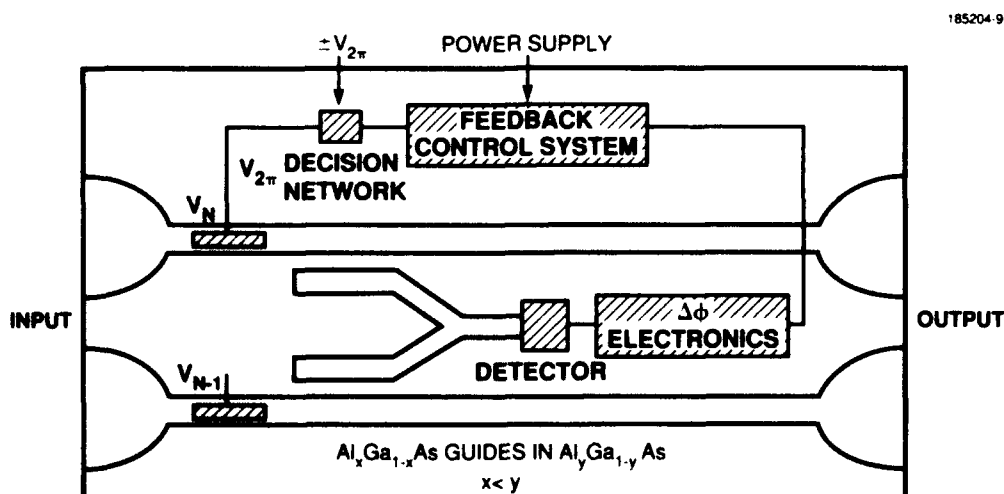


*Figure 1-1. Design of basic module for a proposed integrated optical system that produces a flat-phase output wavefront.*

The Y-junction interferometer technique used for the phase measurement is similar to dither techniques used in optical fiber sensors [4] and phase-locked interferometry [5]. If a sinusoidal phase dither $\Gamma \sin \omega t$ is applied to one arm of a Y-junction interferometer, the detected output power $P_{\Delta\phi}$ is given by

$$P_{\Delta\phi} = \left(P_1 + P_2\right)/2 + \sqrt{P_1 P_2}\, \cos\left(\Delta\phi - \Gamma \sin \omega t\right) \,, \tag{1.1}$$

where $P_1$ and $P_2$ are the powers in the interferometer arms and $\Delta\phi$ is the phase difference between the arms. By using a Bessel function expansion for the cosine-sine term in Equation (1.1), the following expressions for the amplitudes of the first $A(\omega)$ and second $A(2\omega)$ harmonics are obtained:

$$A(\omega) \quad = \quad 2\sqrt{P_1 P_2}\, J_1(\Gamma)\sin\Delta\phi \,, \tag{1.2a}$$

$$A(2\omega) \quad = \quad 2\sqrt{P_1 P_2}\, J_2(\Gamma)\cos\Delta\phi \,, \tag{1.2b}$$

where $J_1(\Gamma)$ and $J_2(\Gamma)$ are Bessel functions of the first kind of order 1 and 2, respectively. The phase difference between the arms can then be calculated using

$$\Delta\phi = \arctan\left(\frac{A(\omega)}{A(2\omega)}\,\frac{J_2(\Gamma)}{J_1(\Gamma)}\right) = \arctan\left(\frac{A(\omega)}{A(2\omega)}\,\frac{\dfrac{\Gamma^2}{8} - \dfrac{\Gamma^4}{96} + \cdots}{\dfrac{\Gamma}{2} - \dfrac{\Gamma^3}{16} + \cdots}\right) \,, \tag{1.3}$$

where the number of significant terms required to evaluate the Bessel functions depends on the amplitude of the phase dither $\Gamma$. Note that the calculated phase difference is independent of the power or power ratio in the input arms of the interferometer.

This technique has been incorporated into a proof-of-concept AlGaAs Mach-Zehnder interferometer, shown in Figure 1-2, to demonstrate phase measurement and correction. The input power is divided between the interferometer arms. Phase modulators are used to apply a sinusoidal phase dither, to set a phase difference between the arms, and to correct the phase difference. A high voltage $V_{abs}$ applied to the fourth modulator creates a power imbalance, by absorbing power in one arm via electroabsorption, in addition to a phase change. The output power $P_{\Delta\phi}$ is detected off chip, the amplitudes of the first and second harmonics are measured, and a computer is used to calculate $\Delta\phi$ from Equation (1.3) and to update $V_{correct}$. The dc output of the interferometer, which is a maximum when $\Delta\phi = 0$, is also monitored. A later version of the interferometer will monolithically integrate the optical and electronic components.

The interferometer was fabricated using a dielectric-loaded strip waveguide structure, illustrated in Figure 1-3. The epilayers were grown by organometallic vapor phase epitaxy, and the rib was etched by chlorine reactive ion etching. The waveguide propagation loss was < 1 dB/cm measured at 870 nm by a Fabry-Perot technique [6]. The abrupt bend insertion loss was ~ 0.20 dB/bend for a 0.5° angle and the Y-junction insertion loss was 0.37 dB for a 1.0° full angle. Phase modulators were fabricated by a selective Be ion implantation, followed by rapid thermal annealing, to form a $p^+$-$n$-$n^+$ structure. The phase in the waveguides was modulated via the electrooptic effect by reverse biasing the $p$-$n$ structure. The $V_\pi$ voltage of these phase modulators was ~ 6.8 V for a 2-mm modulator. The breakdown voltage was ~ 47 V, so a maximum applied voltage of 42 V was chosen for these experiments. The correction voltage was limited to a range slightly larger than $V_\pi/2$ to $5V_\pi/2$, corresponding to a range in phase shift slightly

RATIO
Δφ

FEEDBACK
CONTROL
VOLTAGE

1st
HARMONIC

2nd
HARMONIC

$V_\Gamma \sin\omega t$

$V_{correct}$

INPUT →

$P_{\Delta\phi}$

DETECTOR

DC

$V_{abs}$

$V_{set}$

GENERATE
NEW
$V_{set}$

MONITOR
DC

APPLY
$V_{set}$

MEASURE
1st HARMONIC
AND
2nd HARMONIC

CALCULATE
Δφ
FROM RATIO

Δφ = 0?

YES

NO

UPDATE
$V_{correct}$
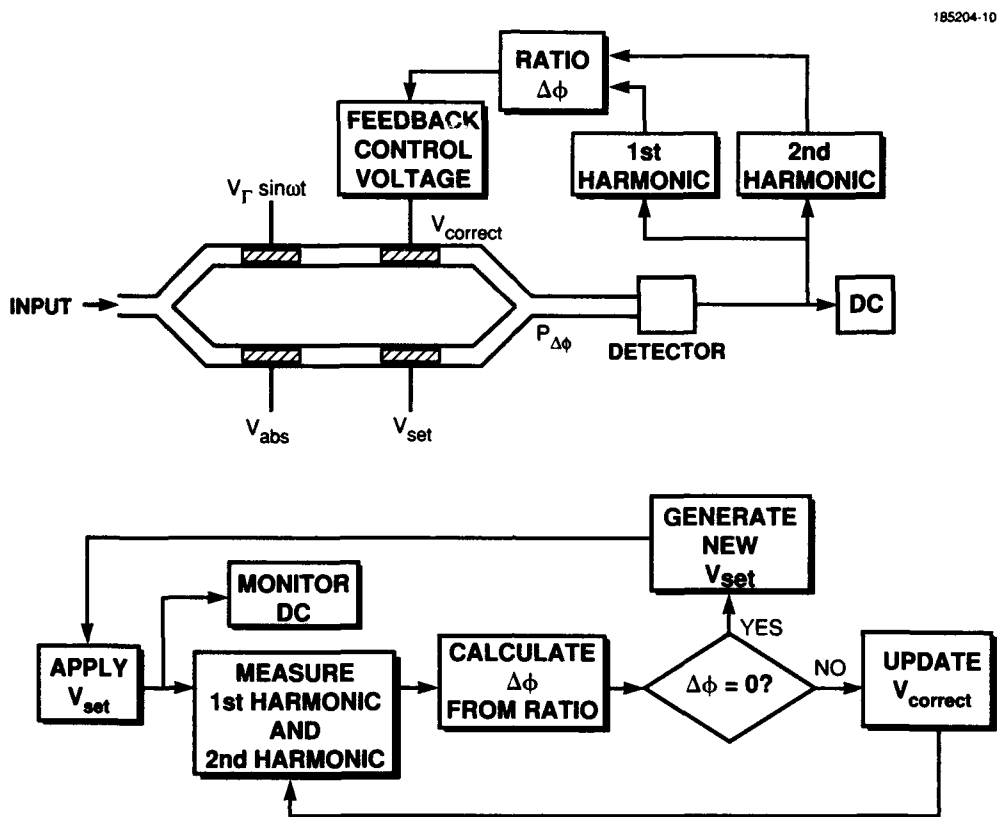
*Figure 1-2. Proof-of-concept AlGaAs Mach-Zehnder interferometer system for demonstrating phase measurement and correction independent of power or power ratio in the interferometer arms.*

larger than $2\pi$. The voltage range chosen ensured that the modulator was always reverse biased and that electroabsorption was small. The sinusoidal phase dither was applied to a 1-mm modulator (with $V_\pi \approx 12.4$ V). Typically, the dither signal had a peak voltage amplitude $V_\Gamma$ of 1.0 V (amplitudes up to 5.0 V have been used) and a frequency of 500 Hz. The Bessel functions in Equation (1.3) were calculated using the first two terms and the simple linear relationship for the amplitude of the phase dither $\Gamma = \pi V_\Gamma / V_\pi$.

The interferometer system was initially operated without feedback to characterize the phase measurement technique as a function of voltage-induced phase differences. A voltage $V_{set}$ was applied to one arm to create a phase difference between the interferometer arms, and the amplitudes of the first and second harmonics were measured and used to calculate $\Delta\phi$. The interferometer dc output was also monitored. As $V_{set}$ was increased above 25 V, a decrease in the peak amplitude of the dc output indicated that the power in the $V_{set}$ arm decreased because of electroabsorption. The phase difference between the interferometer arms was calculated between $-\pi/2$ and $3\pi/2$. The choice of phase range was arbitrary and could be any $2\pi$ range. The calculated $\Delta\phi$ increased linearly with $V_{set}$ over the $-\pi/2$ to $3\pi/2$ range and was in agreement with the observed cosine-squared dependence of the dc output of the interferometer.

3
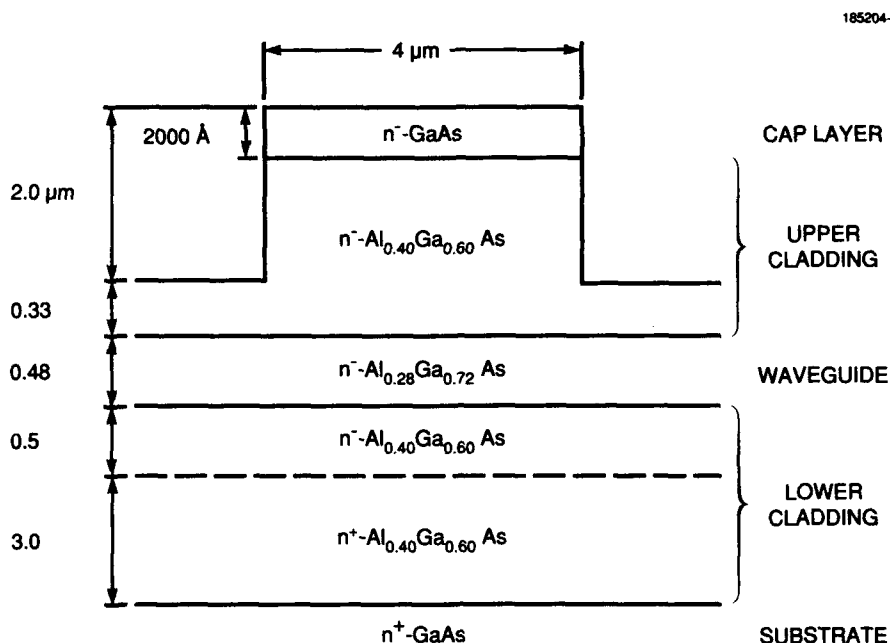
*Figure 1-3. Cross section of the dielectric-loaded strip waveguide structure of the interferometer. In the phase modulator sections, a $p^+$-$n$-$n^+$ structure was used.*

With feedback, as shown in Figure 1-2, a phase difference was again created by applying $V_{set}$, the first and second harmonics were measured, and $\Delta\phi$ was calculated. If $\Delta\phi \neq 0$, then $V_{correct}$ was updated, the harmonics were remeasured, and the new $\Delta\phi$ was calculated. This process was repeated until $\Delta\phi = 0$, that is, until the phase difference between the arms had been corrected. Then, a new $V_{set}$ could be applied and the correction process repeated. The correction voltage was updated by assuming a simple linear relationship between phase and applied voltage: $\Delta\phi$ was divided by $2\pi$ and multiplied by the $V_{2\pi}$ voltage, and this result was added to the old correction voltage. The remainder of the update procedure consisted of limit checks (by adding or subtracting $V_{2\pi}$) to ensure that the correction voltage was within the specified range.

For the case shown in Figure 1-4, $V_{set}$ was increased in successive steps from 0 to 20 V. For each value of $V_{set}$, the first and second harmonics were measured and the phase calculated. Each step in $V_{set}$ resulted in a corresponding increase in the phase difference, followed by phase-correcting cycles until $\Delta\phi = 0$ and phase correction had been attained. As expected, the dc output (not shown) decreased as each $V_{set}$ increment was applied and was maximized when the phase difference was corrected. Figure 1-4(c) shows the updated $V_{correct}$ that was applied to correct the calculated $\Delta\phi$. Note that a $V_{2\pi}$ subtraction was required to keep $V_{correct}$ in the specified range. Phase correction was achieved to an accuracy of 0.0044 rad (or 0.25°). Correction was usually attained in two to three cycles for each step in an applied phase increment. Further improvements could be obtained with more sophisticated algorithms for the phase modulator characteristics (including any nonlinear effects). In this demonstration, the cycle time for each phase-correcting cycle was a few seconds. This can be easily reduced to the order of milliseconds by increasing the dither frequency and using faster feedback electronics.

4
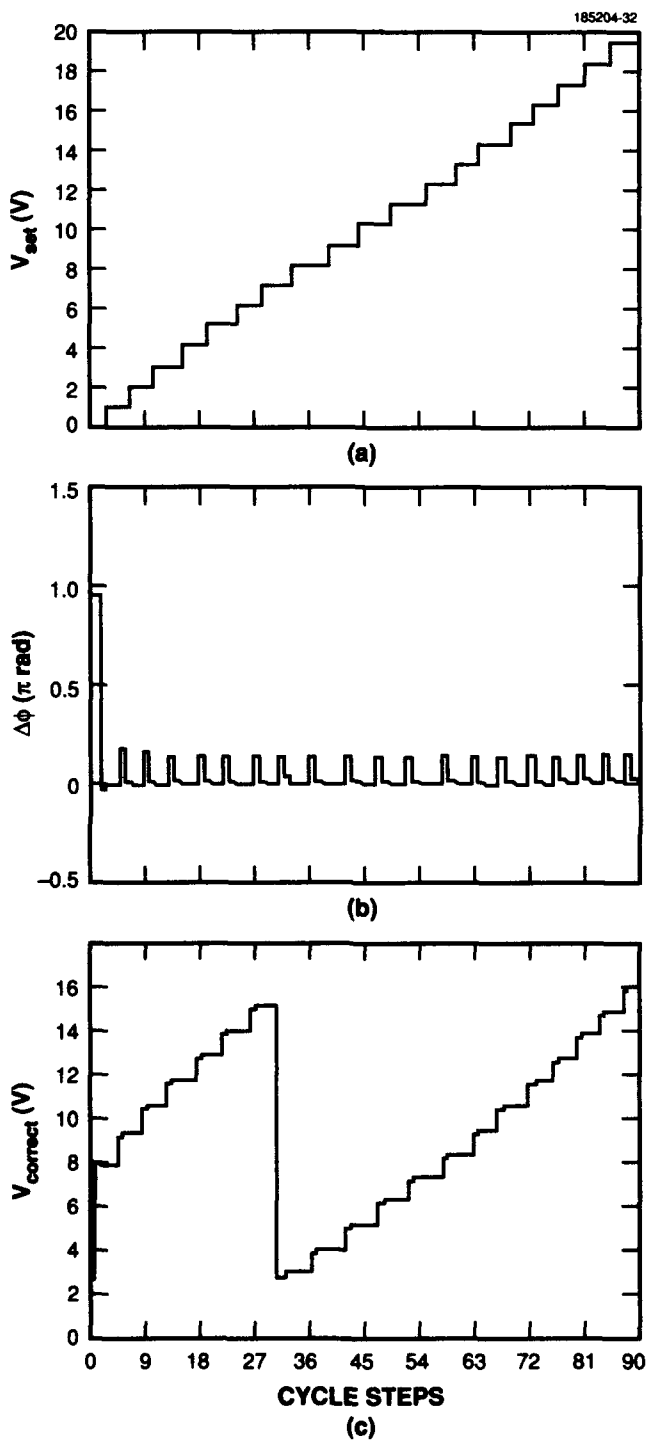
*Figure 1-4. Results for the Mach-Zehnder interferometer system in the feedback mode: (a) applied voltage $V_{set}$ successively stepped from 0 to 20 V, (b) calculated phase difference $\Delta\phi$ between the interferometer arms, and (c) applied correction voltage $V_{correct}$.*

Results were also obtained for the case where a random number generator was used to generate random values for $V_{set}$, which resulted in random phase differences being applied between the interferometer arms. Phase correction again occurred in two to three cycles. Then, as a final test case, $V_{set}$ was increased in successive steps from 20 to 40 V. In this range, in addition to phase change, increased electroabsorption in the $V_{set}$ arm of the interferometer created a power imbalance between the arms. Phase measurement and correction proceeded as usual in two to three cycles with a 30% decrease in the power in one arm, which was observed by monitoring the dc output.

S. D. Lau     R. B. Goodman
J. P. Donnelly     R. H. Rediker
C. A. Wang

## 1.2 TWO-DIMENSIONAL MODEL OF SURFACE-ENERGY-INDUCED MASS TRANSPORT

Recently, mass-transport smoothing of two-dimensional arrays of ion-beam-etched mesas has shown considerable promise for simple fabrication of microoptical structures in compound semiconductors [7]. Previously developed one-dimensional models of mass transport [8],[9], however, cannot be directly applied. Here, we consider the first model of two-dimensional mass transport.

Surface energy per molecule in a curved surface is given by [10]

$$\varepsilon = \alpha v\left(\frac{1}{r} + \frac{1}{r'}\right) , \qquad (1.4)$$

where $\alpha$ is the coefficient of surface tension, $v$ is the molecular volume, and $r$ and $r'$ are the principal radii of curvature. For a slowly varying surface profile, i.e., slopes $\ll 1$, curvature is given by the second derivative of the profile. We further limit our discussions to profiles with proper symmetry such that a Cartesian coordinate system can be conveniently applied. Hence,

$$\varepsilon = -\alpha v\left(\frac{\partial^2 z}{\partial x^2} + \frac{\partial^2 z}{\partial y^2}\right) , \qquad (1.5)$$

where $z$ is the height and $x$ and $y$ are, respectively, the abscissa and ordinate.

Appreciable thermal dissociation occurs at an elevated temperature, and the equilibrium concentration of free atoms in a curved surface is given by [8]–[10]

$$N = N_0\left(1 + \frac{\varepsilon}{kT}\right) , \qquad (1.6)$$

where $N_0$ is the concentration in a flat surface, $k$ is the Boltzmann constant, and $T$ is the absolute temperature. When there is a variation of curvature across the surface, mass transport occurs because of the diffusion and reincorporation of the free atoms and can be described by the continuity equation [8],[9]

$$D\left(\frac{\partial^2 N}{\partial x^2} + \frac{\partial^2 N}{\partial y^2}\right) = \frac{1}{v}\frac{\partial z}{\partial t} , \qquad (1.7)$$

where $D$ is the diffusivity and $t$ is the time. Substituting Equations (1.5) and (1.6) in Equation (1.7), we obtain

$$-\gamma\left(\frac{\partial^4 z}{\partial x^4} + 2\frac{\partial^4 z}{\partial x^2 \partial y^2} + \frac{\partial^4 z}{\partial y^4}\right) = \frac{\partial z}{\partial t} ,\qquad(1.8)$$

where the coefficient $\gamma$ is given by

$$\gamma \equiv \frac{\alpha v^2 N_0 D}{kT} .\qquad(1.9)$$

Note that Equation (1.8) governs the evolution of the surface profile.

Consider a two-dimensional surface profile

$$z = \sum_{m=0}^{\infty} \sum_{n=0}^{\infty} A_{mn} \sin\frac{2m\pi x}{\Lambda_x} \sin\frac{2n\pi y}{\Lambda_y} ,\qquad(1.10)$$

where $\Lambda_x$ and $\Lambda_y$ are the fundamental spatial wavelengths in the $x$ and $y$ directions, respectively. It can readily be shown that Equation (1.8) is satisfied when

$$A_{mn}(t) = A_{mn}(0)e^{-t/\tau_{mn}} ,\qquad(1.11)$$

with the decay time $\tau_{mn}$ given by

$$\frac{1}{\tau_{mn}} = \gamma\left[\left(\frac{2m\pi}{\Lambda_x}\right)^2 + \left(\frac{2n\pi}{\Lambda_y}\right)^2\right]^2 .\qquad(1.12)$$

Note that Equations (1.10) through (1.12) describe the time evolution of the surface profile due to mass transport.

Now consider the simple case in which $\Lambda_x = \Lambda_y \equiv \Lambda$. The higher-order terms in the Fourier expansion will quickly die out owing to the strong dependence of decay time in Equation (1.12). The fundamental term as given by

$$z = A\sin\frac{2\pi x}{\Lambda}\sin\frac{2\pi y}{\Lambda}\qquad(1.13)$$

is represented in a diagram in Figure 1-5. Note that the spacing $\Lambda'$ between the nearest maxima in the diagram is given by

$$\Lambda' = \Lambda / \sqrt{2} ,\qquad(1.14)$$

which is the characteristic distance relevant to the actual device fabrication, i.e., the distance between the etched mesas. We then have from Equation (1.12)

$$\tau = \frac{1}{\gamma}\left(\frac{\Lambda'}{2\pi}\right)^4 ,\qquad(1.15)$$

which is exactly equal to the decay time of a one-dimensional profile with a spatial wavelength $\Lambda'$ [8],[9].
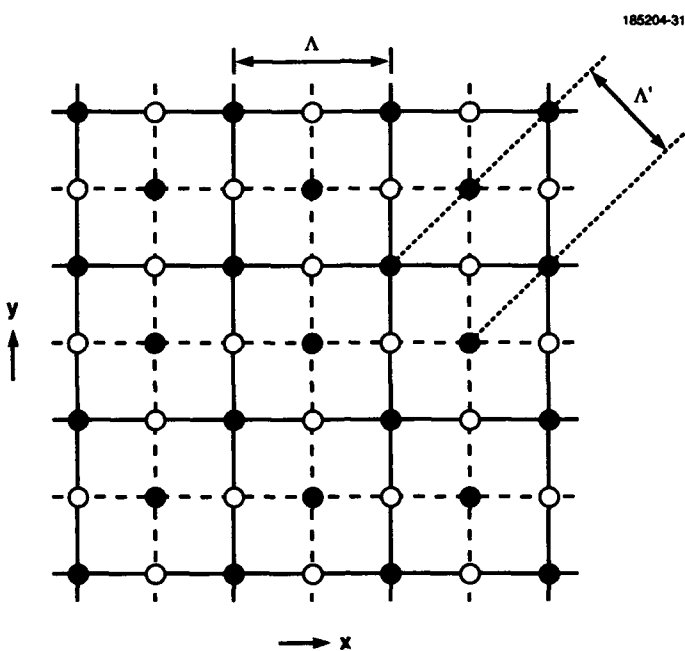
*Figure 1-5. Diagram representing the two-dimensional profile* $z = A \sin(2\pi x/L) \sin(2\pi y/L)$. *The filled and open circles represent the positions of maxima and minima, respectively.*

In the present model, both the coefficient of surface tension $\alpha$ and the surface diffusivity $D$ have been assumed to be isotropic. The dependence of these quantities on crystallographic orientation should be included in a more rigorous treatment. On the other hand, the present model can readily be modified to include diffusion through the vapor phase [11].

<div align="right">Z. L. Liau</div>

## REFERENCES

1.  R. H. Rediker, T. A. Lind, and B. E. Burke, *J. Lightwave Technol.* **6**, 916 (1988).

2.  R. H. Rediker, F. J. Leonberger, and D. P. Greenwood, U.S. Patent No. 4,798,437 (17 January 1989).

3.  D. E. Bossi, W. D. Goodhue, M. C. Finn, K. Rauschenbach, J. W. Bales, and R. H. Rediker, *Appl. Phys. Lett.* **56**, 420 (1990).

4.  T. G. Giallorenzi, J. A. Bucaro, A. Dandridge, G. H. Sigel, Jr., J. H. Cole, S. C. Rashleigh, and R. G. Priest, *IEEE J. Quantum Electron.* **QE-18**, 626 (1982).

5.  G. W. Johnson, D. C. Leiner, and D. T. Moore, *Opt. Eng.* **18**, 46 (1979).

6.  M. W. Austin and P. C. Kemeny, *Integrated Optics* (Springer-Verlag, Berlin, 1985), pp. 140–143.

7.  Z. L. Liau, K. Rauschenbach, and D. E. Mull, unpublished.

<div align="center">8</div>

8.   W. W. Mullins, *J. Appl. Phys.* **30**, 77 (1959).

9.   Z. L. Liau and H. J. Zeiger, *J. Appl. Phys.* **67**, 2434 (1990).

10.  See, for example, L. D. Landau and E. M. Lifshitz, *Statistical Physics* (Addison-Wesley, Reading, Mass., 1958), Chap. 15.

11.  Solid State Research Report, Lincoln Laboratory, MIT, 1991:1, p. 4.

# 2. QUANTUM ELECTRONICS

## 2.1 THREE-WAVELENGTH INTERCONVERSION LASER WITH GAIN AT TWO WAVELENGTHS

Sum-frequency generation from two Nd:YAG lasers operating at 1320 and 1064 nm has aroused significant interest, because the sum-frequency radiation at 589 nm overlaps the strong sodium D-line resonance [1]. Although high average power (up to 20 W) has been obtained, the required laser system is large. An obvious method to make the laser system smaller is to use only one Nd:YAG rod. However, the two transitions use the same upper laser level so lasing at 1064 nm, which has much higher gain, quickly robs gain at 1320 nm [2]. Consequently, the use of only one laser rod with intracavity sum-frequency generation results in inefficient and unstable operation.

We have successfully circumvented this problem by using a filter to block 1064-nm lasing in the absence of a nonlinear crystal. With the nonlinear crystal, the laser can operate at 1064 nm by sum-frequency generation of 1064 and 1320 nm to 589 nm, which transmits through the filter, reflects off the end mirror, and regenerates 1064 nm by difference-frequency generation, allowing further amplification at 1064 nm. Although the 1064-nm radiation robs gain from the 1320-nm transition, the 1064-nm radiation requires the presence of 1320-nm radiation for the parametric processes, so the laser tends to optimize 589-nm radiation. This new technique has directly and stably generated as much as 1 mJ/pulse of 589-nm radiation at a 10-Hz repetition rate. We expect even higher energies to be available. In this report, we describe the laser cavity and preliminary experiments to probe the laser dynamics in this new mode of operation.

Figure 2-1 shows a schematic of the laser. For 1320-nm operation, this laser operates in a conventional fashion. Flashlamps invert the $Nd^{3+}$ ions in the gain medium to provide a single-pass unsaturated gain of ~ 2 at 1320 nm (in contrast to 30 at 1064 nm). Mirrors at each end of the cavity with reflectivities



| 1320 nm | MIRROR, $R_1$ | WINDOW | WINDOW | MIRROR, $R_1'$ |
| 1064 | MIRROR, $R_2$ | WINDOW | MIRROR | |
| 589 | | MIRROR | WINDOW | MIRROR, $R_3'$ |
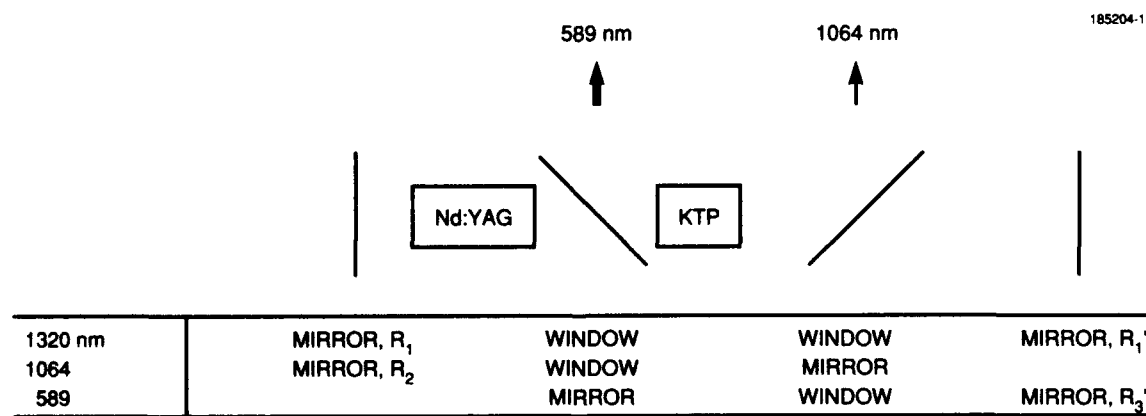
*Figure 2-1. Schematic of the three-wavelength parametric conversion laser. The KTP crystal is cut and oriented for phase matching to generate the sum frequency 589 nm from 1064 and 1320 nm. The Nd:YAG crystal is pumped by flashlamps to provide gain at 1064 and 1320 nm. Characteristics of the optics at each of the three wavelengths are given below the figure.*

$R_1 = 0.5$ and $R_1' = 0.7$ provide feedback for the lasing. When the laser is operated above the 1320-nm threshold, the new form of operation is also possible. In the left half of the laser cavity (see Figure 2-1), the laser has high gain for 1064 nm. The 1064- and 1320-nm radiation are partially converted to 589-nm radiation in the KTP crystal. The 589- and 1320-nm radiation pass through a filter that reflects the residual 1064-nm radiation out of the laser cavity. After back reflection, the 589-nm radiation is partially converted in the KTP crystal to 1064- and 1320-nm radiation. The 589-nm radiation that is not down-converted becomes the sum-frequency output from the laser.

The threshold for the new mode of operation is determined by the need for the round-trip gain at 1064 nm, including up-conversion to 589 nm and down-conversion back again, to be $> 1$:

$$\chi_u \chi_d R_2 R_3' G_1^2 > 1 , \qquad (2.1)$$

where $\chi_u$ and $\chi_d$ are the efficiencies of up-conversion and down-conversion, respectively, $G_1$ is the single-pass gain for 1064 nm through the Nd:YAG crystal while saturated by the 1320-nm operation, $R_2$ is the reflectivity for 1064 nm at the left end of the cavity, and $R_3'$ is the reflectivity for 589 nm at the right end. $R_3'$ was chosen to be 1, but $R_2$ was chosen to be 0.2 because parasitic lasing at 1064 nm was found to deplete the inversion for higher reflectivities. If $G_1$ is not strongly saturated by 1320-nm operation, the up-conversion and down-conversion efficiencies do not have to be higher than 0.1.

In the limit of no depletion of the 1320-nm radiation, the product of the parametric up-conversion and down-conversion efficiencies is given by [3]

$$\chi_u \chi_d = \sin^4\left(k E_2 l / 2\right) , \qquad (2.2)$$

where $k$ is a constant that includes the nonlinear coefficient for the parametric process, $E_2$ is the electric field associated with the 1320-nm radiation, and $l$ is the length of the nonlinear crystal. To reach threshold for the new mode of operation, significant intensity at 1320 nm is necessary to produce a sufficiently large $\chi_u \chi_d$. On the other hand, for $G_1$ to be as large as possible, it is important that the 1320-nm radiation not saturate the inversion too strongly. Thus, the yellow light generation was observed only when the cavity was lossy at 1320 nm. Although this simple theory provides insight into the threshold condition for the new mode of operation, it cannot provide guidance for maximizing the 589-nm output when there is significant depletion of the 1320-nm radiation.

The time sequence for light at 1320 and 589 nm is shown in Figure 2-2. Three relaxation oscillations are observed for the 1320-nm radiation. During the first two oscillations, 1064- and 589-nm radiation is generated. The intensity of the third relaxation oscillation is too weak to allow efficient parametric conversion between the 589- and 1064-nm radiation, so the threshold condition [Equation (2.1)] is not satisfied.

Figure 2-3 shows detailed time behavior at 1320 and 589 nm during the first relaxation oscillation. Initially, the 1320-nm radiation builds up, which is a prerequisite to efficient parametric conversion between 589 and 1064 nm. The most efficient parametric conversion appears for the highest intensity 1320-nm radiation, which occurs during one of the spikes in the multilongitudinal mode behavior. At the peak of the 589-nm output, the biggest multimode spike in the 1320-nm output is no longer observed. Apparently, the 589-nm radiation significantly depletes the spike in the 1320-nm radiation. If such

12

*Figure 2-2. Time sequence of 1320-nm (upper) and 589-nm (lower) radiation. The relaxation oscillations following flashlamp pumping are shown. The time scale is 2 µs/div.*
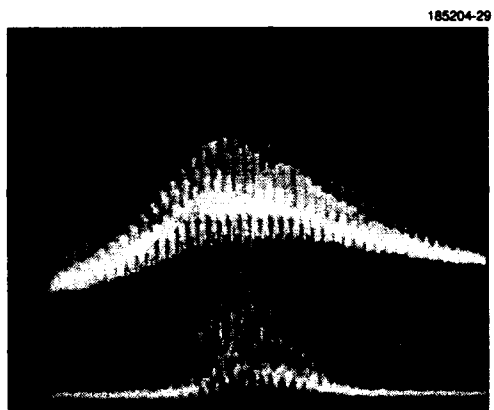


*Figure 2-3. Detail of a single relaxation oscillation for 1320-nm (upper) and 589-nm (lower) radiation. The time scale is 50 ns/div.*

depletion could be maintained for the round-trip in the laser cavity, efficient energy conversion would be obtained. Therefore, this new technique may be capable of generating 589-nm radiation more efficiently than sum-frequency generation from two different lasers [1].

The detailed dynamics of 1064- and 589-nm outputs are shown in Figure 2-4. These two outputs have the same time behavior, showing that they are locked together through the parametric process. The differences are a slight time shift that occurs because of the different optical paths to the detectors and
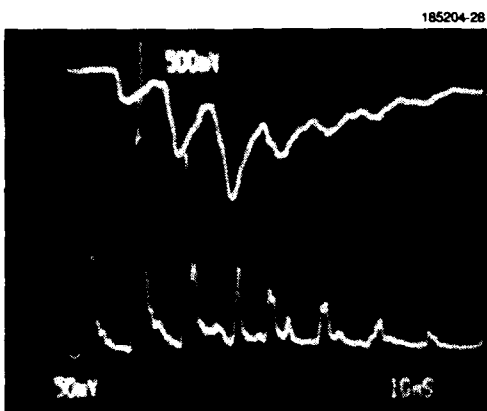
*Figure 2-4. Further detail showing 1064-nm (upper) and 589-nm (lower) radiation. The time scale is 10 ns/div. The 1064-nm radiation trace shows increasing intensity downward.*

a smearing of the 1064-nm trace because a slower detector was used. For the initial buildup the 589-nm radiation occurs in a very narrow spike associated with the largest spike of the 1320-nm radiation. The energy in the 1320-nm spike is quickly depleted, which forces the 589-nm spike to broaden. Surprisingly, in only seven round-trips the 589-nm radiation evolves from a very narrow (< 1 ns) pulse to continuous operation.

P. A. Schulz

T. H. Jeys

## 2.2 FREQUENCY TUNING OF MICROCHIP LASERS USING PUMP-DIODE MODULATION

Changes in pump power are well known to cause frequency changes in the output of diode-pumped solid state lasers. As the pump power increases, more thermal energy is deposited in the gain medium, raising its temperature and changing both the refractive index and the cavity length. Each of these effects contributes to changing the resonant frequency of the laser cavity and therefore the frequency of the laser output. Because frequency tuning via pump-diode modulation relies on thermal effects, it is often thought to be too slow for most applications, including frequency or phase locking of a laser. In addition, modulating the pump power has the undesirable effect of changing the amplitude of the laser output.

Here the frequency response to pump-diode modulation is analyzed for a microchip laser. The response is sufficiently fast for phase locking the laser, as has been demonstrated experimentally [4]. It is shown that in a microchip laser a large frequency modulation can be obtained with only a small amount of amplitude modulation, making pump-diode modulation a viable technique for several applications requiring frequency-agile lasers. Furthermore, pump-diode modulation has advantages over other commonly used frequency modulation techniques, such as piezoelectric and electrooptic tuning, that make it preferable for some applications: it requires very little power, no high voltage electronics, no special mechanical fixturing, and no additional intracavity elements that can degrade the laser performance.

Another reason that it is important to understand the frequency response of the microchip laser to changes in pump-diode power is that such power fluctuations are often responsible for a large portion of the frequency fluctuations of the laser output. The frequency response function characterizes this component.

Before proceeding, aspects of the microchip laser relevant to the following discussion will be reviewed. Microchip lasers [5] are small monolithic laser cavities created by polishing a piece of gain medium flat and parallel on two sides. Dielectric cavity mirrors are then deposited on the two polished surfaces. The lasers are longitudinally pumped by a butt-coupled diode laser. The cavity lengths of microchip lasers are typically comparable to, or shorter than, the absorption length of the gain medium at the pump wavelength. Efficient pump absorption is obtained by reflecting the pump beam off the output coupler (the cavity mirror furthest from the diode), thereby doubling the path length of the pump in the gain medium. The transverse dimensions of the oscillating mode in the cavity are determined by the temperature profile induced by pump absorption and are much smaller than the transverse dimensions of the gain medium. As a result of the way the transverse mode is defined, the oscillating mode is concentric with the pump beam.

In the following analysis, approximations are made based on the characteristics of the laser cavity. Both the pump beam and oscillating mode, which are modeled as Gaussian with constant amplitude and diameter, propagate along the cavity axis. Because the thermal conductivity of the gain medium of interest (Nd:YAG) is much greater than the thermal conductivity of the dielectric mirrors and of air, it is assumed that all heat flow is directed in the plane normal to the cavity axis. The above assumptions reduce the thermal analysis to a two-dimensional problem. To further simplify the analysis, the transverse dimensions of the gain medium are initially modeled as infinite. A discussion of the effect of heat sinking the gain medium at a finite distance from the cavity axis is given later.

With the above approximations, the frequency response of the microchip laser to pump-diode modulation can be solved in closed form. The resonant frequency of a laser cavity changes with cavity length according to the relationship

$$\frac{dv}{v} = -\frac{dl_{op}}{l_{op}} , \tag{2.3}$$

where $v$ is the lasing frequency (nominally $v = v_0$) and $l_{op}$ is the optical length (length $l$ times refractive index $n$) of the laser cavity. The variation in optical cavity length as a function of temperature is given by

$$dl_{op} = nl\left(\alpha_e + \frac{1}{n}\frac{\partial n}{\partial T}\right) dT_{ave} , \tag{2.4}$$

where $\alpha_e$ is the thermal expansion coefficient and $T_{ave}$ is the temperature averaged over the volume of the laser mode of waist size $r_m$:

$$T_{ave} = \frac{2}{\pi r_m^2 l}\int_0^l\int_0^{2\pi}\int_0^{\infty} T \exp\left(-\frac{2r^2}{r_m^2}\right) r\, dr\, d\theta\, dz . \tag{2.5}$$

The temperature distribution $T$ within the gain medium satisfies the equation

$$\frac{dT}{dt} = \alpha \nabla^2 T + \frac{Q}{\rho c} ,$$ (2.6)

where $c$ is the specific heat, $\rho$ is the density, $\alpha = k/\rho c$ is the thermal diffusivity, $k$ is the thermal conductivity, and $Q$ is the rate of heat deposition per unit volume. The spectral components of the rate of heat deposition $Q(\omega,r)$ are proportional to the change in pump power $P(\omega)$ at frequency $\omega$:

$$Q(\omega,r)\sin(\omega t) = \frac{2\kappa P(\omega)}{\pi r_m^2 l} \exp\left(-\frac{2r^2}{r_p^2}\right)\sin(\omega t) ,$$ (2.7)

where $\kappa$ is the heat-generating efficiency of the pump and $r_p$ is the radius of the pump mode.

To solve the above equations we will start with the known temperature profile resulting from a unit impulse excitation at time $t = 0$ and position $r = 0$:

$$h(t,r) = \frac{1}{4\pi k t} \exp\left(-\frac{r^2}{4\alpha t}\right) .$$ (2.8)

By convolving this impulse response with the Gaussian spatial thermal excitation profile per unit pump power, $Q(\omega,r)/P(\omega)$, we obtain

$$h_G(t,r) = \frac{2\kappa}{\pi \rho c l \left(r_p^2 + 8\alpha t\right)} \exp\left(-\frac{2r^2}{r_p^2 + 8\alpha t}\right) .$$ (2.9)

Next, we perform the averaging over the oscillating mode volume, resulting in the expression

$$h_G(t)_{ave} = \frac{2\kappa}{\pi \rho c l \left(r_m^2 + r_p^2 + 8\alpha t\right)} .$$ (2.10)

To obtain $T(\omega)_{ave}$, we convolve this function with the time dependence of the thermal excitation and multiply by $P(\omega)$, yielding

$$T(\omega)_{ave}\sin[\omega t + \phi(\omega)] = \frac{\kappa P(\omega)}{4\pi k l}$$

$$\times \left\{ \left[\frac{\pi}{2} - \mathrm{Si}\left(\frac{\omega}{\omega_0}\right)\right]\cos\left[\omega\left(t+\frac{1}{\omega_0}\right)\right] + \mathrm{Ci}\left(\frac{\omega}{\omega_0}\right)\sin\left[\omega\left(t+\frac{1}{\omega_0}\right)\right] \right\} ,$$ (2.11)

where

$$\omega_0 = \frac{8\alpha}{r_m^2 + r_p^2}$$ (2.12)

and Si and Ci are the sine and cosine integrals. The frequency response of the laser to pump-power

16

modulation is, therefore,

$$\left|\frac{dv(\omega)}{dP(\omega)}\right|\sin\left[\omega t + \phi(\omega)\right] = \frac{v_0\kappa}{4\pi kl}\left(\alpha_e + \frac{1}{n}\frac{\partial n}{\partial T}\right)$$

$$\times \left\{\left[\frac{\pi}{2} - \mathrm{Si}\left(\frac{\omega}{\omega_0}\right)\right]\cos\left[\omega\left(t + \frac{1}{\omega_0}\right)\right] + \mathrm{Ci}\left(\frac{\omega}{\omega_0}\right)\sin\left[\omega\left(t + \frac{1}{\omega_0}\right)\right]\right\}. \qquad (2.13)$$

The magnitude and phase of this frequency response function are shown in Figure 2-5. Asymptotically,

$$\lim_{\omega \gg \omega_0}\left|\frac{dv(\omega)}{dP(\omega)}\right| = \frac{v_0\kappa}{4\pi kl}\left(\alpha_e + \frac{1}{n}\frac{\partial n}{\partial T}\right)\frac{\omega_0}{\omega}, \qquad (2.14a)$$

$$\lim_{\omega \gg \omega_0}\phi(\omega) = \frac{\pi}{2}, \qquad (2.14b)$$

$$\lim_{\omega \ll \omega_0}\left|\frac{dv(\omega)}{dP(\omega)}\right| = \frac{v_0\kappa}{4\pi kl}\left(\alpha_e + \frac{1}{n}\frac{\partial n}{\partial T}\right)\left|\gamma + \ln\left(\frac{\omega}{\omega_0}\right)\right|, \qquad (2.14c)$$

$$\lim_{\omega \ll \omega_0}\phi(\omega) = \pi, \qquad (2.14d)$$

where $\gamma \approx 0.577$ is Euler's constant.

The logarithmic divergence of the response function for small $\omega$ is a result of the approximation that the gain medium has infinite transverse dimensions. To examine the response for low-frequency modulation, we solve the above equations in the steady-state limit, with a radially symmetric (infinite) heatsink at a distance $r_b$ from the cavity axis. The solution to the steady-state ($\omega = 0$) diffusion Equation (2.6) is

$$T(0,r) = T_b + \frac{\kappa P(0)}{4\pi kl}\left\{\mathrm{Ei}\left(-\frac{2r^2}{r_p^2}\right) - \mathrm{Ei}\left(-\frac{2r_b^2}{r_p^2}\right) - \ln\left(\frac{r^2}{r_b^2}\right)\right\}, \qquad (2.15)$$

where $T_b$ is the temperature of the heatsink and Ei is the exponential integral. The average temperature seen by the oscillating mode is obtained by changing the upper limit of the radial integration in Equation (2.5) to $r_b$. The result is

$$T(0)_{\mathrm{ave}} = T_b + \frac{\kappa P(0)}{4\pi kl}$$

$$\times \left\{\gamma + \ln\left(\frac{2r_b^2}{r_m^2 + r_p^2}\right) + \mathrm{Ei}\left[-\frac{2r_b^2\left(r_m^2 + r_p^2\right)}{r_m^2 r_p^2}\right] - \mathrm{Ei}\left(-\frac{2r_b^2}{r_m^2}\right) - \mathrm{Ei}\left(-\frac{2r_b^2}{r_p^2}\right)\right\}. \qquad (2.16)$$

17
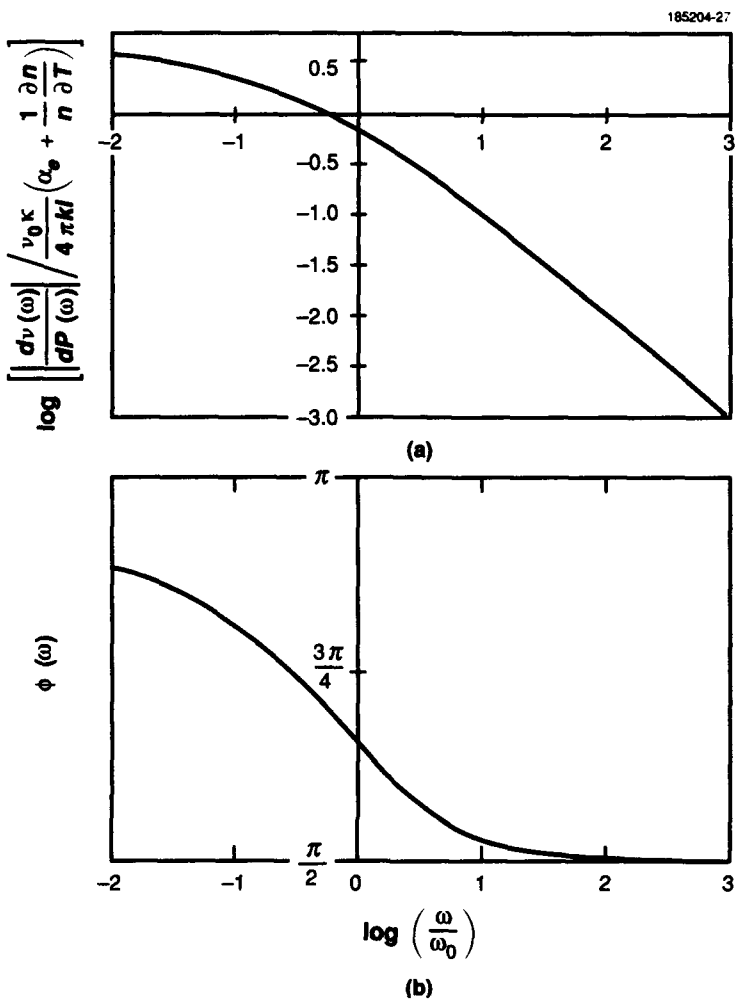
Figure 2-5. The (a) magnitude and (b) phase of the frequency response function of a microchip laser to pump-power modulation.

For a quasi-static change in pump power ($\omega \leq \omega_{qs}$, with $\omega_{qs}$ to be defined below), the change in laser frequency is

$$\frac{dv\left(\omega_{qs}\right)}{dP\left(\omega_{qs}\right)} = -\frac{v_0 \kappa}{4\pi kl}\left(\alpha_e + \frac{1}{n}\frac{\partial n}{\partial T}\right)$$

$$\times \left\{\gamma + \ln\left(\frac{2r_b^2}{r_m^2 + r_p^2}\right) + \text{Ei}\left[-\frac{2r_b^2\left(r_m^2 + r_p^2\right)}{r_m^2 r_p^2}\right] - \text{Ei}\left(-\frac{2r_b^2}{r_m^2}\right) - \text{Ei}\left(-\frac{2r_b^2}{r_p^2}\right)\right\} . \qquad (2.17)$$

18
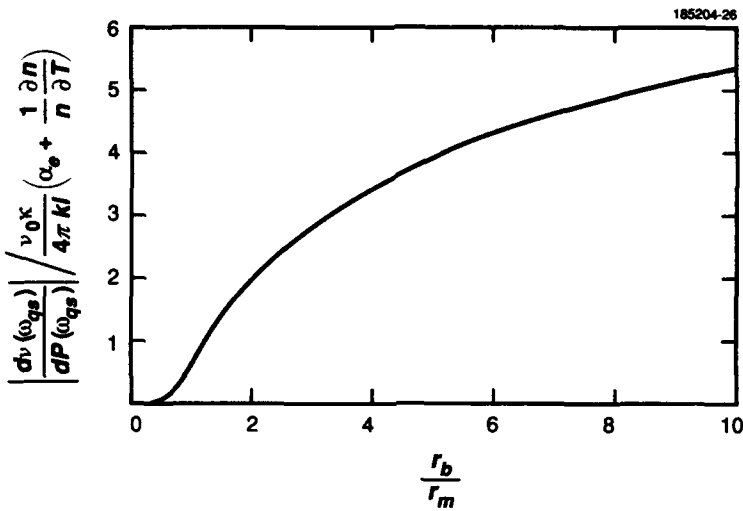
*Figure 2-6. Magnitude of the quasi-static frequency response of a microchip laser to pump-power modulation as a function of $r_b$ for $r_m = r_p$.*

This function is illustrated in Figure 2-6. Asymptotically,

$$\lim_{r_b \gg r_m, r_p} \frac{dv(\omega_{qs})}{dP(\omega_{qs})} = -\frac{v_0 \kappa}{4\pi k l}\left(\alpha_e + \frac{1}{n}\frac{\partial n}{\partial T}\right)\left\{\gamma + \ln\left(\frac{2r_b^2}{r_m^2 + r_p^2}\right)\right\} .$$  (2.18)

In this limit, and in the limit $\omega_{qs} \ll \omega_0$, Equation (2.17) is equivalent to Equation (2.13) if

$$\omega_{qs} = \frac{4\alpha}{r_b^2}e^{-2\gamma} .$$  (2.19)

Equation (2.19) can be interpreted as defining the quasi-static frequency limit. For modulation frequencies below $\omega_{qs}$, the response function is approximately given by Equation (2.17); at higher modulation frequencies Equation (2.13) becomes more accurate.

A very important aspect of the frequency response function is its dependence on the dimensions of the laser. The characteristic frequencies of the system, $\omega_0$ and $\omega_{qs}$, increase as $1/(r_m^2 + r_p^2)$ and $1/r_b^2$, respectively. For the highest frequency response, all the transverse dimensions should be kept as small as possible. The magnitude of the response function is inversely proportional to the cavity length. This also means that, for a laser with a given slope efficiency, the ratio of the frequency modulation to amplitude modulation [$FM(\omega)/AM(\omega)$] for a given pump modulation increases as the inverse of the cavity length. For large $FM(\omega)/AM(\omega)$, the cavity length should be kept as short as possible.

19

With its short cavity length (typically $l < 1$ mm) and small transverse dimensions ($r_m$, $r_p \approx 0.1$ mm, $r_b \approx 0.5$ mm), the microchip laser is ideally suited for frequency tuning via pump-diode modulation. (Its output frequency is also extremely sensitive to pump-power noise.) For a Nd:YAG microchip laser ($\rho = 4.55$ g cm$^{-3}$, $c = 0.6$ J g$^{-1}$ K$^{-1}$, $k = 0.103$ W cm$^{-1}$ K$^{-1}$, $\alpha_e + \partial n/n\partial T = 1.15 \times 10^{-5}$ K$^{-1}$) operating at 1.32 $\mu$m ($\kappa \approx 0.2$), with the dimensions indicated above, $|d\nu(\omega_{qs})/dP(\omega_{qs})| = 16$ MHz mW$^{-1}$, $f_{qs} = \omega_{qs}/2\pi = 3$ Hz, and $f_0 = \omega_0/2\pi = 240$ Hz. These numbers are in good agreement with experiment [4]. The magnitude of the frequency response is sufficiently large to make pump-diode power modulation an effective means of frequency tuning the microchip laser.

J. J. Zayhowski

## REFERENCES

1.  T. H. Jeys, A. A. Brailove, and A. Mooradian, *Appl. Opt.* **28**, 2588 (1989).

2.  H. E. Tomaschke, G. A. Henderson, D. A. Thompson, J. S. Brookman, and R. E. Juhala, *Conf. Lasers Electro-Optics, 1990 Tech. Dig. Ser.*, Vol. 7 (Optical Society of America, Washington, D.C., 1990), p. 252.

3.  A. Yariv, *Quantum Electronics*, 3rd ed. (Wiley, New York, 1989), p. 427.

4.  J. J. Zayhowski and J. A. Keszenheimer, to be published *IEEE J. Quantum Electron.* **28** (1992).

5.  J. J. Zayhowski and A. Mooradian, *Opt. Lett.* **14**, p. 24 (1989).

# 3. MATERIALS RESEARCH

## 3.1 GaAs-BASED DIODE LASERS ON Si WITH INCREASED LIFETIME OBTAINED BY USING A STRAINED InGaAs ACTIVE LAYER

GaAs-based diode lasers fabricated on Si substrates are attractive as potential components for optical interconnects between Si VLSI circuits. The development of such lasers has been hindered by the high dislocation density ($> 10^6$ cm$^{-2}$) and strain ($\sim 10^9$ dyn cm$^{-2}$) that are present in GaAs layers grown on Si substrates, because of the differences between the two materials in lattice parameter and thermal expansion, respectively. Although room-temperature CW operation of GaAs/AlGaAs diode lasers on Si substrates has been achieved by several groups, the longest lifetime previously reported for such lasers is 17 h [1], which was obtained for devices with many strain-relieving microcracks.

For quantum-well diode lasers fabricated on GaAs substrates, improvement in reliability has been obtained by replacing the GaAs active layer with a strained InGaAs layer [2]–[4]. The improvement is believed to result from the incorporation of In, which retards the propagation of dark-line defects because the In atom is larger than the Al, Ga, and As atoms, all of which are almost the same size [5]. We now report the first fabrication of InGaAs/AlGaAs strained quantum-well lasers on Si substrates. One $In_{0.05}Ga_{0.95}As$/AlGaAs graded-index separate-confinement heterostructure (GRIN-SCH) laser operated CW for 56.5 h at room temperature. The longest lifetime we have obtained for similar GaAs/AlGaAs devices on Si is only 75 min [6].

The substrates used for laser fabrication were $n^+$ wafers oriented 3° off (100) towards (110). A 2-$\mu$m-thick $n^+$-GaAs buffer layer was grown on each wafer by organometallic vapor phase epitaxy (OMVPE) at Spire Corporation. The wafer was first cleaned in situ by heating to 1000°C in $H_2$. A thin GaAs film was nucleated at 400°C, a layer $\sim 1$ $\mu$m thick was grown at 675°C, and the remainder of the buffer was then grown by the thermal-cycled growth (TCG) process [7] in order to reduce the dislocation density. In this process a GaAs layer is grown at 675°C, then annealed at 900°C. The temperature is lowered to near room temperature, then raised to 675°C, and a new cycle is begun. In the present study, five layers, each 200 nm thick, were grown by TCG. For GaAs/AlGaAs GRIN-SCH lasers on Si wafers, we have found [8] that employing TCG reduces the threshold current density by about half and increases the differential quantum efficiency by about 30%.

The wafer was then transferred to an OMVPE system at Lincoln Laboratory for growth of the following layers: 0.1-$\mu$m-thick $n^+$-GaAs, 10-nm-thick $n^+$-$In_{0.1}Ga_{0.9}As$ defect filtering, 1-$\mu$m-thick $n$-$Al_{0.7}Ga_{0.3}As$ cladding, 0.15-$\mu$m-thick $n$-$Al_xGa_{1-x}As$ confining ($x$ linearly graded from 0.7 to 0.2), 6-nm-thick $In_yGa_{1-y}As$ active ($y = 0.02$ or 0.05), 0.15-$\mu$m-thick $p$-$Al_xGa_{1-x}As$ confining ($x$ linearly graded from 0.2 to 0.7), 1-$\mu$m-thick $p$-$Al_{0.7}Ga_{0.3}As$ cladding, and 0.1-$\mu$m-thick $p^+$-GaAs cap.

Broad-stripe lasers, 100 $\mu$m wide, have been fabricated and tested under pulsed conditions at room temperature. The emission wavelengths of the $In_{0.02}Ga_{0.98}As$ and $In_{0.05}Ga_{0.95}As$ lasers are $\sim 855$ and 870 nm, respectively. For both types of lasers, the internal quantum efficiency is $\sim 80\%$ and the loss coefficient $\sim 5$ cm$^{-1}$. Figure 3-1 shows the threshold current density $J_{th}$ of these lasers as a function of cavity length $L$.
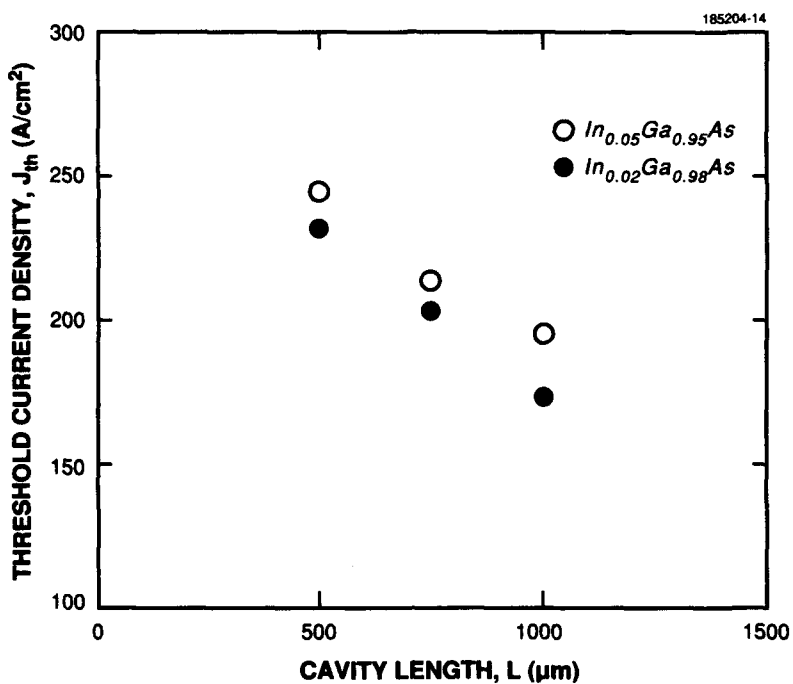
*Figure 3-1. Threshold current density $J_{th}$ as a function of cavity length L for $In_{0.02}Ga_{0.98}As/AlGaAs$ and $In_{0.05}Ga_{0.95}As/AlGaAs$ strained quantum-well lasers.*

For $L = 1000\,\mu m$, the values of $J_{th}$ are 174 and 195 $A/cm^2$ for $In_{0.02}Ga_{0.98}As$ and $In_{0.05}Ga_{0.95}As$ lasers, respectively. These are the lowest values so far reported for semiconductor lasers fabricated on Si substrates. For the same $L$, the value of $J_{th}$ is lower for $In_{0.02}Ga_{0.98}As$ lasers than for $In_{0.05}Ga_{0.95}As$ lasers, the opposite dependence on In content from that observed for InGaAs lasers on GaAs substrates. For the lasers on Si substrates, it is believed that the higher strain associated with greater In content causes an increase in the number of threading dislocations that are bent into the active layer, producing the observed increase in $J_{th}$.

Gain-guided lasers with a 5-$\mu m$ stripe were mounted junction side up on copper heatsinks for CW operation. For devices 500 $\mu m$ long, the threshold current is $\sim 50$ mA. Several devices were operated CW at a constant output power of 2 mW/facet at a heatsink temperature of 22°C. For $In_{0.02}Ga_{0.98}As$ lasers, the longest lifetime was 4 h. The current increased at a rate of $\sim 40$ mA/h in the first 2 h and by $\sim 70$ and 130 mA in each of the next 2 h. For $In_{0.05}Ga_{0.95}As$ lasers, the degradation rate was considerably lower and the lifetime considerably longer. The current required to maintain constant power for one of these lasers is plotted against time in Figure 3-2. The current increased by 22 mA in the first hour. The rate of increase subsequently decreased, reaching 3 mA/h after 10 h, but then gradually increased over the remainder of the device lifetime, reaching about 10 mA/h at 56.5 h, when the current was 330 mA.

All the InGaAs lasers on Si degraded gradually until the threshold current became too high to permit laser operation. In contrast, failure of similar devices with a GaAs active layer was associated with a sharp increase in the degradation rate, which presumably resulted from the propagation of dark-line defects. Because the degradation rate was lower for $In_{0.05}Ga_{0.95}As$ lasers than for $In_{0.02}Ga_{0.98}As$ lasers,
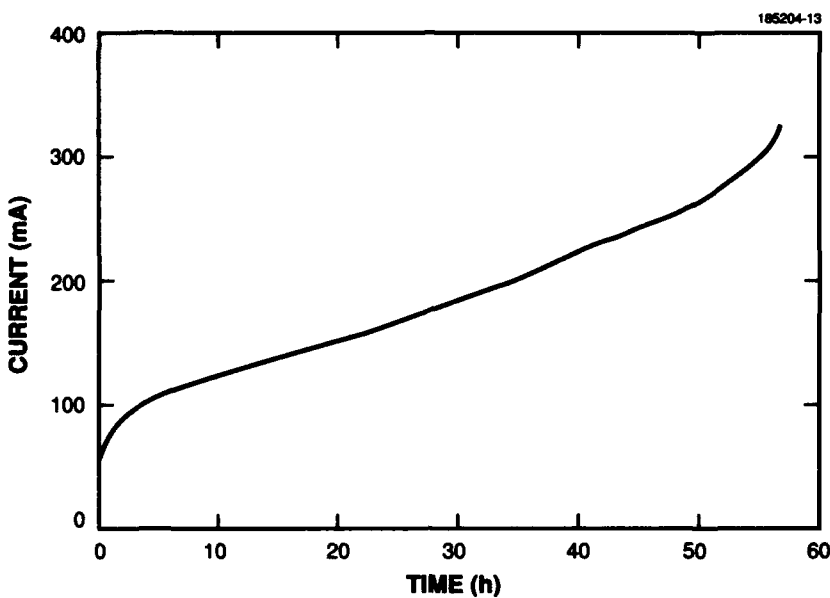
*Figure 3-2. Time dependence of current required to maintain a constant power of 2 mW/facet for an $In_{0.05}Ga_{0.95}As/AlGaAs$ laser at a heatsink temperature of 22°C.*

it should be possible to obtain longer lifetimes by still further increasing the In content in the active layer. However, there will be an optimum value for the In content because the threshold current will eventually become too high as a result of the increased bending of threading dislocations caused by increasing strain.

H. K. Choi
C. A. Wang

## REFERENCES

1.  D. G. Deppe, D. C. Hall, N. Holonyak, Jr., R. J. Matyi, H. Shichijo, and J. E. Epler, *Appl. Phys. Lett.* **53**, 874 (1988).

2.  R. G. Waters, D. P. Bour, S. L. Yellen, and N. F. Ruggieri, *IEEE Photon. Technol. Lett.* **2**, 531 (1990).

3.  S. E. Fischer, R. G. Waters, D. Fekete, J. M. Ballantyne, Y. C. Chen, and B. A. Soltz, *Appl. Phys. Lett.* **54**, 1861 (1989).

4.  D. P. Bour, D. B. Gilbert, K. B. Fabian, J. P. Bednarz, and M. Ettenberg, *IEEE Photon. Technol. Lett.* **2**, 173 (1990).

5.  J. Matsui, *Proc. Mater. Res. Soc. Symp.* **14**, 477 (1983).

6.  H. K. Choi, C. A. Wang, and N. H. Karam, *IEEE Photon. Technol. Lett.* **3**, 289 (1991).

7.  B-Y. Tsaur, J. C. C. Fan, G. W. Turner, F. M. Davis, and R. P. Gale, *Proc. 16th IEEE Photovoltaic Specialists Conf.* (IEEE, New York, 1982), p. 1143 .

8.  H. K. Choi, C. A. Wang, and J. C. C. Fan, *J. Appl. Phys.* **68**, 1916 (1990).

# 4. SUBMICROMETER TECHNOLOGY

## 4.1 POLYSILYNES AS DRY-DEVELOPED RESISTS FOR 193-NM EXCIMER LASER LITHOGRAPHY

New photoresist processes for use at 193 nm have been constrained by the high optical density of the common polymeric resins used for longer wavelengths. As a result, new resist processes have employed either surface imaging [1] or bilayers [2]–[5]. Most bilayer resists contain silicon to improve their etch resistance in subsequent process steps, and at longer wavelengths they are wet developed [6],[7]. We report here on a process for dry development of the silicon-containing polysilynes following excimer laser exposure at 193 nm. The development anisotropy requires the latent image to be formed only at the resist surface, rather than throughout the full thickness of the resist, thereby relaxing requirements for the resist's optical density and the imaging depth of focus.

The polysilynes are a unique class of Si-backbone polymers where each silicon is bound to three other silicon atoms, forming a three-dimensional network [8]. The molecular weight, solubility, and various other properties of these materials are dictated by the pendant R-group. Strong ultraviolet absorbance in the polysilynes results from the $\sigma$-$\sigma^*$ electronic transition in the Si backbone. Other $\sigma$-conjugated polymers, such as the linear polysilanes, exhibit quantum efficiencies for Si-Si bond scission in solution that approach unity [9]. These values have not been measured for the polyalkylsilynes, but they are expected to be similarly high. When irradiation is performed in air, photooxidation of the Si-Si network occurs, resulting in formation of a rigid, insoluble siloxane.

Figure 4-1 shows Auger electron spectroscopy (AES) results of poly(cyclohexylsilyne-co-$n$-butylsilyne) exposed to various 193-nm laser doses. The peak locations for elemental silicon and $SiO_2$ are indicated on the figure; a shift toward lower kinetic energies occurs with increasing exposure dose, indicative of the oxidation of the polymer. The atomic composition of poly($n$-butylsilyne) exposed to 100 mJ/cm$^2$ was measured to be $Si_{1.0}O_{1.34}C_{1.99}$ using AES. Note the surprisingly low C/Si ratio (the C/Si ratio is > 4 in the original polymer) resulting from alkyl-group photodesorption [10]. Infrared spectroscopic studies have also been performed [10] and indicate that the structure of the photolyzed product is a three-dimensional siloxane, intermediate in properties between a true polysiloxane and $SiO_2$. This oxidized product results from oxygen insertion into each Si-Si bond, so that each silicon is bound to three oxygens. The average stoichiometry for such a material is $SiO_{1.5}$ (because each oxygen is shared by two silicons). As mentioned earlier, the oxidized polysilyne had a stoichiometry of $SiO_{1.34}$, which is close to this value, further supporting our assertion about the nature of the oxidized product.

The dry-developed resist process relies on the selective etching of unexposed polysilyne. Various plasma chemistries have been studied for selective dry etching of Si over $SiO_2$ [11]–[13]. Chlorine is a good choice for the $Si/SiO_2$ system [11], as atomic chlorine inserts into Si-Si bonds but is too weak an oxidant to attack the stronger Si-O bonds. However, using chlorine we have observed poor selectivity for polysilynes, presumably because of the presence of the weaker Si-alkyl bonds in the exposed as well as the unexposed areas. Therefore, a weaker oxidant such as bromine is better suited to optimize etch selectivity between photooxidized and virgin polysilyne films. The actual chemistry leading to etch
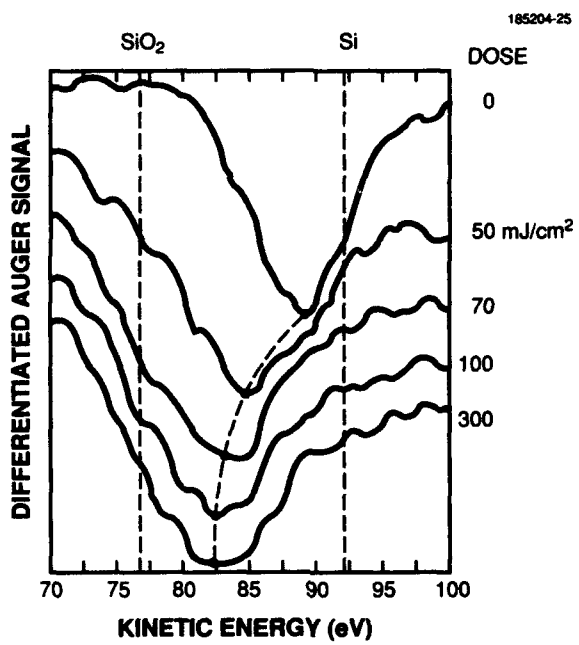
*Figure 4-1. Auger electron spectra of the Si LMM transition for poly(cyclohexylsilyne-co-n-butylsilyne) exposed at 193 nm to various doses as indicated.*

selectivity in polysilynes is more complex than the case of $Si/SiO_2$, however. Nakamura et al. [13] have observed that the poly-$Si/SiO_2$ etch selectivity can vary by a factor of 300, depending on the levels of carbon present in the plasma reactor. The lowest levels of selectivity reported were between 10:1 and 20:1 and occurred when levels of carbon in the plasma were highest, i.e., in the presence of a hydrocarbon resist masking layer. For polysilyne etching, we have found that the type as well as the amount of carbon residing in the film is as important as the photooxidation efficiency in realizing optimum resist sensitivity and contrast. For example, poly(phenylsilyne) (PPSy) exhibits very poor etch selectivity owing to the presence of the phenyl group. The aromatic carbon ring composing the phenyl group is very stable and only slowly attacked by bromine. As a result, the decomposition and etching of the phenyl moiety are rate limiting for both the oxidized and virgin PPSy. The net effect is a reduction in the HBr etch selectivity between virgin and oxidized PPSy.

The etching tools used in our studies were two parallel-plate RF reactive ion etchers (RIEs). The first, used for the bulk of the studies, was typically run at −60-V bias and 25-W power. The second was equipped with independently powered top and bottom electrodes, a temperature-controlled stage, and variable electrode spacing. This etcher could be run at as low as −40-V bias. Etch rates of unexposed polysilynes in HBr plasma in either etcher typically ranged from 5 to 40 nm/min.

26
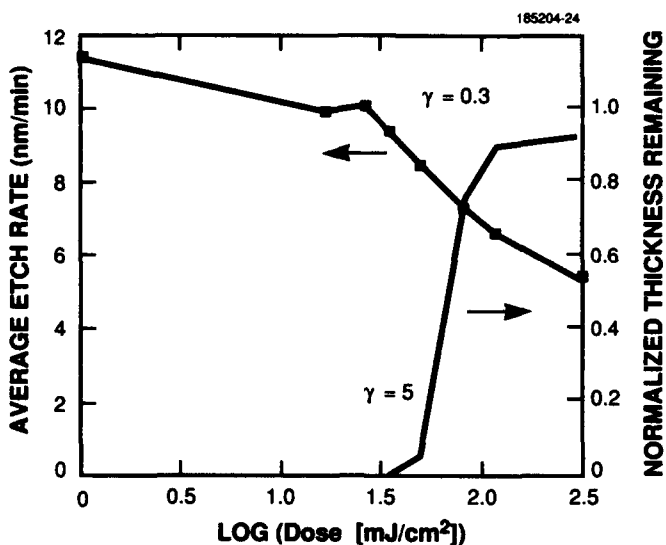
*Figure 4-2. Average etch rate of poly(cyclohexylsilyne-co-n-butylsilyne) with HBr RIE at –60-V bias (left axis) and normalized thickness remaining in a poly(cyclohexylsilyne-co-n-butylsilyne)/novolac bilayer after HBr development at –60-V bias followed by $O_2$ RIE (right axis). Indicated on each curve are the respective contrast values.*

The polysilyne etch rate as a function of 193-nm exposure dose was obtained by irradiating thick (0.3 to 0.8 $\mu$m) samples of the polysilyne resist and then etching in HBr. The etch rates, which were depth averaged, were obtained using mechanical stylus profilometry. This method can be misleading, however, since the HBr etch rate is reduced by laser exposure only in the top 30 nm [10]. Nevertheless, the average etch rates can be useful for determining resist sensitivity and optimizing development times. Figure 4-2 shows etch rate data for poly(cyclohexylsilyne-co-$n$-butylsilyne) etched at –60-V bias in HBr. The contrast is calculated to be 0.3, but the $O_2$ RIE step following the HBr step raises the process contrast to 5 because of the > 50:1 etch selectivity of the carbon-based planarizer vs the polysilyne with $O_2$ RIE.

For high resolution patterning we used a 193-nm, 5:1, 0.32-numerical-aperture projection imaging system with a 4-mm-diam field. Figure 4-3 shows a scanning electron micrograph of poly(cyclohexylsilyne-co-$n$-butylsilyne) patterned at 90 mJ/cm$^2$ and developed with HBr RIE at –60-V bias followed by $O_2$ RIE of the planarizing layer. The bilayer consisted of 0.75-$\mu$m-thick hard-baked AZ photoresist (the planarizer) and a 100-nm-thick polysilyne imaging layer. High-aspect-ratio, straight-walled profiles with nominal 0.2-$\mu$m lines and spaces are obtained in this process.

R. R. Kunz       R. R. Paladugu

M. W. Horn       D. C. Shaver

R. B. Goodman
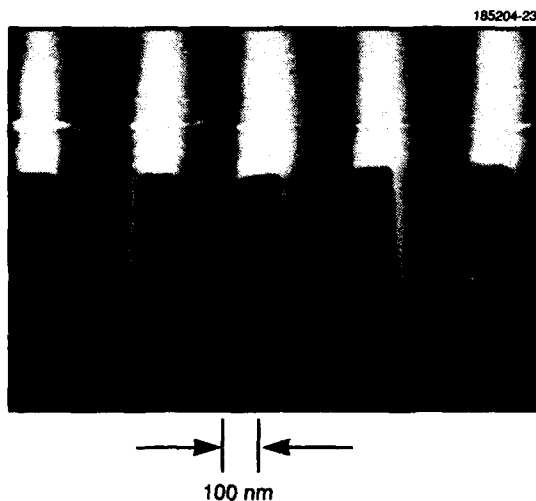
*Figure 4-3. 0.2-µm line-and-space features printed in 100-nm-thick poly(cyclohexylsilyne-co-n-butylsilyne). Development was with HBr RIE at –60-V bias; pattern transfer was with $O_2$ RIE.*

## 4.2 DIAMOND COLD CATHODES

Robust, high-current-density (> 1000 A cm$^{-2}$) cold cathodes, if they could be made, would have wide application in high power, high frequency devices. Three approaches have been taken to fabricate such cathodes. The first uses high electric fields produced at sharp edges or tips to cause electrons to tunnel out of a metal into vacuum [14]. However, at high current densities these electric-field-assisted cathodes are unreliable and prone to catastrophic failure [14]. The second approach uses conventional semiconductors, such as Si [15], GaAs [16], or some organic crown ethers [17], with metals like K or Cs to produce a material in which the conduction band is either above or very close to the vacuum energy level. With appropriate biasing of $n$-$p$ junctions in the semiconductor, electrons can be ejected from the conduction band into vacuum. Although such devices can emit very high current densities (> 1500 A cm$^{-2}$), they are easily contaminated and will not operate after exposure to $O_2$ [15]. The third approach uses wide-bandgap (> 5 eV) materials, including MgO [18], SiO$_2$ [19], and diamond [20]–[22], that have their conduction band within 1 eV of the vacuum energy level, even in the presence of $O_2$ and H$_2$O. Most of these materials are unacceptable for high-current-density cathodes, because they are insulators owing to low charge-carrier concentrations, low mobilities, and high trap densities. However, diamond can be doped either $n$- or $p$-type [23],[24] and grown with sufficient quality to have low trap densities and high carrier mobilities, making it a semiconductor instead of an insulator [24]. We report here on the fabrication and characterization of diamond cold cathodes. We believe electron emission is the result of the conduction band in diamond being above the vacuum energy level.

The diamond cold cathodes were produced by forming diodes in $p$-type semiconducting diamond using carbon ion implantation into heated (320°C) substrates, as described by Prins [25]. A current density of 10$^{-5}$ A cm$^{-2}$ was used, with ion energies of 50, 106, and 170 keV and fluences of 3.8 × 10$^{16}$,

28

$3 \times 10^{16}$, and $3.5 \times 10^{16}$ cm$^{-2}$, respectively. The substrates were then coated with 1 $\mu$m of electron-beam-evaporated Al, which was patterned into $60 \times 60$-$\mu$m squares on 100-$\mu$m centers using standard photolithography. The resistance between Al squares and to the $p$-type substrate was ~ $10^2$ to $10^3$ $\Omega$ and ohmic in character. The substrates were then etched to a depth of 1.1 $\mu$m with ion-beam-assisted etching [26], using the Al squares as a mask to form mesa structures consisting of Al, carbon-implanted diamond, and substrate, as shown in Figure 4-4. After etching, all the structures exhibited diode character to the $p$-type substrate with breakdown voltages of 400 to 600 V. The substrates were then mounted in either indium or silver-doped epoxy, cleaned in an oxygen plasma, and rinsed in water and acetone.

For measurements of emitted current the mesa-etched diodes were characterized in a turbopumped vacuum probing station with a base pressure of ~ $1 \times 10^{-5}$ Torr. The anode consisted of a stainless steel sheet that was coated with colloidal graphite and placed about a millimeter above the diode under test. For the initial experiments the diode-substrate structures were forward biased to $V_D = -100$ to $-200$ V, most of which was dropped across the high resistance of the substrate. In later experiments $V_D$ was reduced to $> -100$ V by heating the structure to 100°C, which reduced the substrate resistance by a factor of ~ 4. When a diode was forward biased, a negative current appeared on the anode, which varied with diode current $I_D$ and anode voltage $V_A$, as shown in Figures 4-5 and 4-6, respectively. The anode current $I_A$ is usually noisy and decreases with time, becoming too low to measure ($< 5 \times 10^{-13}$ A) after a few minutes. When the emitted current from one diode is too small to measure the other diodes still emit, and if the substrate is cleaned, as previously described, all the diodes again emit. If $O_2$ is leaked into the probing station to ~ $1 \times 10^{-2}$ Torr, the emission current increases and no longer decreases with time. When the $O_2$ leak is turned off and the probing system returns to its base pressure, the emission current substantially increases but remains noisy, as shown in Figure 4-7. The addition of $H_2$ has little to no effect on emission current.

Several experiments were performed to determine the important parameters for electron emission and to characterize the carbon-implanted diodes. Current emission was observed in all the diodes fabricated in (111)- and (100)-oriented diamond substrates with acceptor densities ~ $10^{16}$ cm$^{-3}$ (determined from capacitance measurements) and in chemical-vapor-deposited homoepitaxial diamond [24] with estimated boron concentrations of $10^{19}$ cm$^{-3}$. Mesa-etched Al-diamond Schottky diodes, fabricated as described earlier but without carbon implantation, did not emit current when forward biased to the same voltage and current levels as the implanted diodes. By varying the substrate temperature from 25 to 100°C and keeping $I_D$ constant, $V_D$ could be varied from $-200$ to $-100$ V. To within experimental error, a factor of 3, $I_A$ is independent of $V_D$. Diodes fabricated in insulating, type IIa diamond exhibited no forward or emitted current when forward biased ($V_D = -100$ V). Modified diodes were formed by etching 230 nm into the carbon-implanted substrate, thereby removing the dark conductive layer formed during carbon implantation. Without the conductive layer, the $60 \times 60$-$\mu$m Al squares formed diodes to the substrate and back-to-back diodes to each other. After the substrate was etched a second time to form mesas, as previously described, the diodes exhibited current-voltage characteristics nearly identical to the unmodified diodes and still emitted current when forward biased. Figure 4-8 shows $I_D$ as a function of $V_D$ for the carbon-implanted and Al-diamond Schottky diodes.
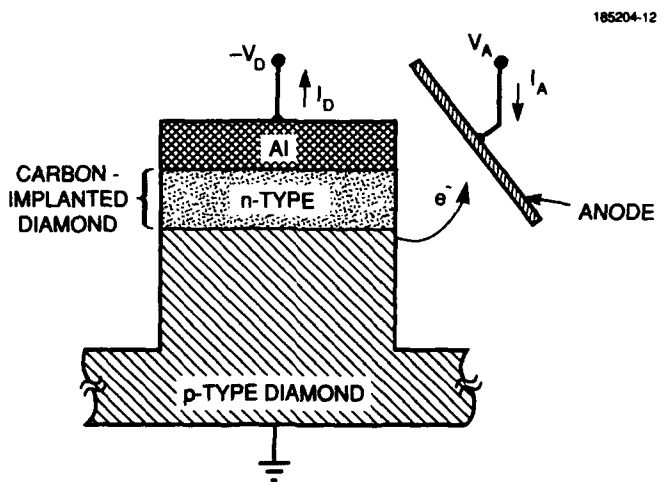
Figure 4-4. Schematic drawing of the mesa-etched cold cathode diode.
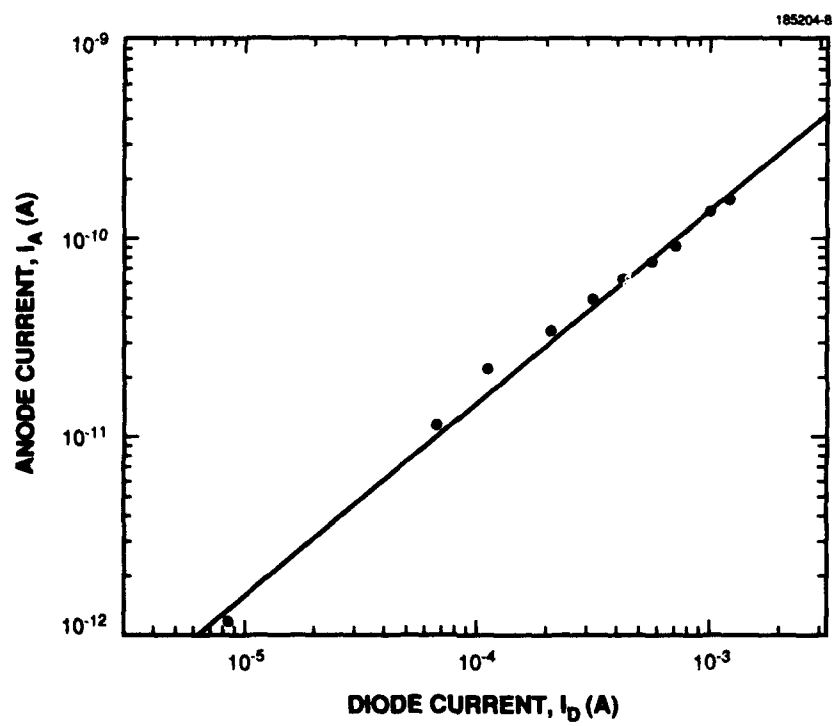


Figure 4-5. $I_A$ as a function of $I_D$ for $V_D$ = -60 to -100 V and $V_A$ = 100 V.

30
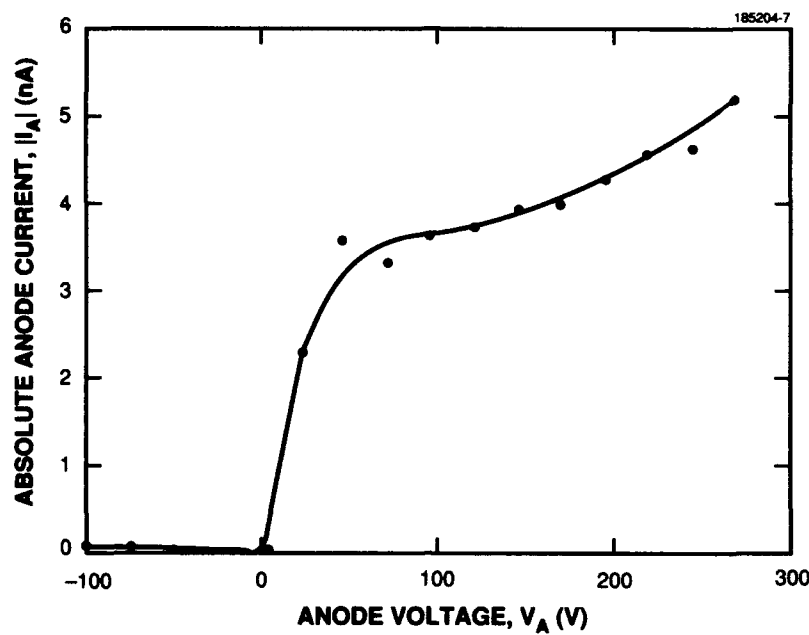
*Figure 4-6. Absolute value of $I_A$ as a function of $V_A$ for $I_D = 1$ mA.*
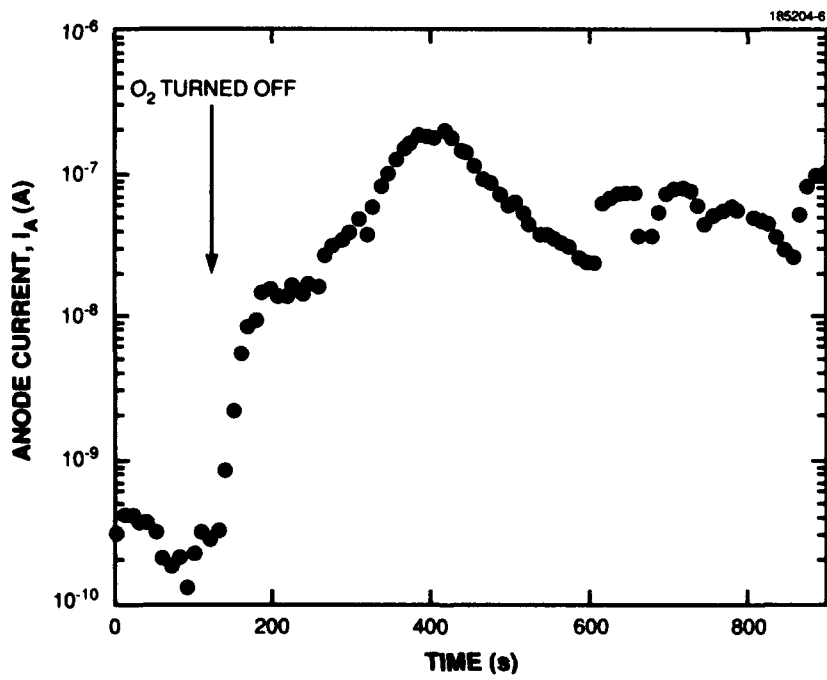


*Figure 4-7. $I_A$ as a function of time for $I_D = 10$ mA, $V_A = 100$ V, and $V_D = -60$ to $-200$ V depending on diode temperature. At 100 s, the pressure in the vacuum probing system was changed from $\sim 10^{-2}$ Torr of $O_2$ to a base pressure of $1 \times 10^{-5}$ Torr.*
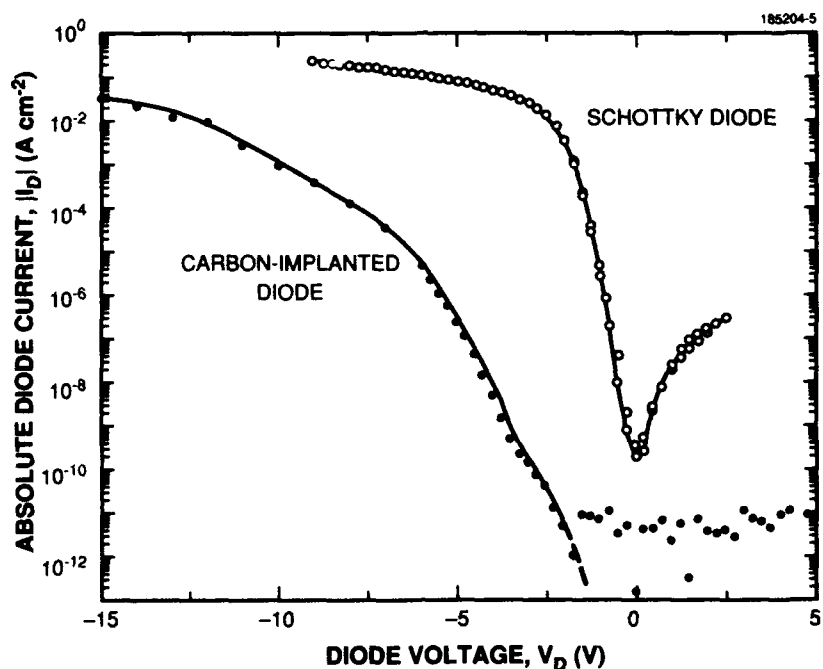
*Figure 4-8. Absolute value of $I_D$ as a function of $V_D$ at 25°C for the carbon-implanted diode (dots) shown schematically in Figure 4-4 and for an Al-diamond Schottky diode (open circles) fabricated without carbon implantation. Both diodes were formed on type IIb, (111)-oriented diamonds with acceptor concentrations ~ 1 × 10^{16} cm^{-3}. To minimize current transients, probably caused by traps in the carbon-implanted diode, the voltage was maintained on this diode for 30 min before the current measurement was taken. The leakage current of the ion-implanted diodes was below the resolution of the measurement system, ~ 10^{-11} A cm^{-2}, for bias voltages $V_D$ from –2 to 17 V.*

These results indicate that current flow through the diode is required for current emission and that Al-diamond Schottky diodes with a barrier height of < 2 eV will not emit electrons. The dark conductive layer formed during carbon implantation, which is similar to graphite [27] with a resistivity of ~ 8 × $10^{-3}$ Ω cm and a temperature coefficient of $-4 \times 10^{-6}$ Ω cm°C$^{-1}$, is not required for current emission. The large forward voltage (~ 2 V) required for the carbon-implanted diode to conduct, shown in Figure 4-8, indicates that the carbon-implanted diodes are not Schottky in character and may be $n$-$p$ junctions, as speculated by Prins [25]. We conjecture that when the diodes are forward biased, electrons are injected into the $p$-type diamond from the ion-damaged $n$-type region just below the dark conductive layer. Once the electrons are in the $p$-type semiconductor they can be emitted into vacuum. Similar models are used to explain cold cathode diodes [28].

In summary, we have formed cold cathodes in diamond by fabricating mesa-etched diodes using carbon ion implantation into $p$-type substrates. When these diodes are forward biased, current is emitted into vacuum. The cathode efficiency (emitted current divided by diode current) varies from $2 \times 10^{-4}$ to $1 \times 10^{-10}$ and increases with the addition of $O_2$ to the vacuum system. If a minority carrier lifetime < 500 ps [29] and an electron mobility < 1000 cm$^2$ V$^{-1}$ s$^{-1}$ are assumed, then the minority carrier diffusion length is < 1 $\mu$m. If the emitting area is the perimeter of the diode (240 $\mu$m) times the minority carrier diffusion length, then the

32

current density is estimated to be 0.1 to 1 A cm$^{-2}$ for an instrument-limited $I_D = 10$ mA. This compares favorably with Si cold cathodes (not coated with Cs), which have efficiencies of $\sim 2 \times 10^{-5}$ and current densities of $\sim 2 \times 10^{-2}$ A cm$^{-2}$ [30]. We believe that higher current densities and efficiencies can be obtained with an increase in $I_D$, more efficient cathode designs, and an ultrahigh-vacuum environment.

M. W. Geis            M. Marchywka*

N. N. Efremow         D. G. Socker*

J. D. Woodhouse       J. F. Hochedez*

M. D. McAleese

*Author not at Lincoln Laboratory.

## REFERENCES

1.  M. A. Hartney, R. R. Kunz, D. J. Ehrlich, and D. C. Shaver, *Proc. SPIE* **1262**, 119 (1990).

2.  R. R. Kunz, P. A. Bianconi, M. W. Horn, R. R. Paladugu, D. C. Shaver, D. A. Smith, and C. A. Freed, *Proc. SPIE* **1466**, 218 (1991).

3.  M. W. Horn, S. W. Pang, and M. Rothschild, *J. Vac. Sci. Technol. B* **8**, 1493 (1990).

4.  S. W. Pang, R. R. Kunz, M. Rothschild, R. B. Goodman, and M. W. Horn, *J. Vac. Sci. Technol. B* **7**, 1624 (1989).

5.  R. R. Kunz, M. Rothschild, D. J. Ehrlich, S. P. Sawan, and Y. G. Tsai, *J. Vac. Sci. Technol. B* **7**, 1629 (1989).

6.  G. M. Wallraff, R. D. Miller, N. Clecak, and M. Baier, *Proc. SPIE* **1466**, 211 (1991).

7.  K. Nate, A. Mizushima, and H. Sugiyama, *Proc. SPIE* **1466**, 206 (1991).

8.  P. A. Bianconi and T. W. Weidman, *J. Am. Chem. Soc.* **110**, 2342 (1988).

9.  R. D. Miller and J. Michl, *Chem. Rev.* **89**, 1359 (1989).

10. R. R. Kunz, M. W. Horn, P. A. Bianconi, D. A. Smith, and C. A. Freed, *J. Vac. Sci. Technol. A* **9**, 1447 (1991).

11. G. C. Schwartz and P. M. Schiable, *J. Vac. Sci. Technol.* **16**, 410 (1979).

12. T. D. Bestwick and G. S. Oehrlein, *J. Vac. Sci. Technol. A* **8**, 1696 (1990).

13. M. Nakamura, K. Iizuka, and H. Yano, *Jpn. J. Appl. Phys.* **28**, 2142 (1989).

14. C. A. Spindt, C. E. Holland, A. Rosengreen, and I. Bodie, to be published in *Proc. 3rd Int. Conf. Vacuum Microelectronics* (IEEE, New York, 1991).

15. G. G. P. van Gorkom and A. M. E. Hoeberechts, *J. Vac. Sci. Technol. B* **4**, 108 (1986).

16. J. J. Scheer and J. van Laar, *Solid State Commun.* **3**, 189 (1965).

17.  J. L. Dye, *Science* **247**, 663 (1990).

18.  M. O. Aboelfotoh and J. A. Lorenzen, *J. Appl. Phys.* **48**, 4754 (1977).

19.  R. Wilaims, *Phys. Rev.* **144**, 588 (1966).

20.  F. J. Himpsel, J. A. Knapp, J. A. VanVechten, and D. E. Eastman, *Phys. Rev. B* **20**, 624 (1979).

21.  B. B. Pate, B. J. Waclawaski, P. M. Stefan, C. Binns, T. Ohta, M. H. Hecht, P. J. Jupiter, M. L. Shek, D. T. Pierce, N. Swanson, R. J. Celotta, G. Rossi, I. Lindau, and W. E. Spicer, *Physica B* **117/118**, 783 (1983).

22.  M. W. Geis, J. A. Gregory, and B. B. Pate, *IEEE Trans. Electron Devices* **38**, 619 (1991).

23.  K. Okano, H. Kiyota, T. Iwasaki, Y. Nakamura, Y. Akiba, T. Kurosu, M. Iida, and T. Nakamura, *Appl. Phys. A* **51**, 1731 (1991).

24.  M. W. Geis, *Proc. Mater. Res. Soc. Symp.* **162**, 15 (1990).

25.  J. F. Prins, *Appl. Phys. Lett.* **41**, 950 (1982).

26.  N. N. Efremow, M. W. Geis, D. C. Flanders, G. A. Lincoln, and N. P. Economou, *J. Vac. Sci. Technol. B* **3**, 416 (1985).

27.  J. F. Prins, *Radiat. Eff. Lett.* **76**, 79 (1983).

28.  R. L. Bell, *Negative Electron Affinity Devices* (Clarendon, Oxford, 1973), pp. 96–109.

29.  P.-T. Ho, C. H. Lee, J. C. Stephenson, and R. R. Cavanagh, *Opt. Commun.* **46**, 202 (1983).

30.  J. Y. Ea, B. Lalevic, D. Zhu, Y. Lu, and R. J. Zeto, *IEEE Electron Device Lett.* **11**, 403 (1990).

# 5. HIGH SPEED ELECTRONICS

## 5.1 $CO_2$ LASER MODULATOR BASED ON INTERSUBBAND TRANSITIONS OF PHOTOGENERATED ELECTRONS IN QUANTUM WELLS

Intersubband transitions in semiconductor quantum wells have been explored extensively in recent years. One of the advantages of these transitions is that they can be designed to occur over a broad range of wavelengths in the infrared. Intersubband transitions are being used as the basis for detectors [1], far-infrared lasers [2], and absorption modulators for $CO_2$ lasers [3]. The conduction electrons required in these devices are usually provided by modulation doping. An alternative technique for introducing electrons into the quantum wells is the cross-gap absorption of light [4]. We have used this technique to demonstrate a $CO_2$ laser absorption modulator having a strong modulation capability and low cross-gap pump power requirements.

The cross-gap pumping technique is well suited for an absorption modulator because the electron density and hence the absorption strength can be varied over a large range. A schematic diagram of this technique is shown in Figure 5-1. The cross-gap radiation generates electron-hole pairs in the lowest-order conduction and valence subbands in the quantum well. The electrons are then free to undergo transitions to the second conduction subband for a duration determined by the cross-gap recombination time. Because the intersubband relaxation time of electrons ($\tau_{ISB} \leq 1$ ps) is significantly shorter than the cross-gap recombination time ($\tau_{CG} \geq 1$ ns), each photogenerated electron can undergo many intersubband transitions before recombining.

The modulator in the present study consists of 100 7-nm-wide GaAs quantum wells separated by 22-nm-wide $Al_{0.28}Ga_{0.72}As$ barriers. This multiple quantum well (MQW) structure was grown by organo-metallic vapor phase epitaxy on a semi-insulating GaAs substrate. The background electron density in the MQW region was determined from capacitance-voltage measurements to be ~ $1.4 \times 10^{16}$ $cm^{-3}$. Infrared absorption measurements made on this sample show a 6-meV-wide intersubband absorption line centered at a wavelength of ~ 10.8 $\mu$m. This linewidth is about half of that seen in more heavily doped quantum wells and is thought to result from lower ionized impurity scattering in the present sample.

After growth a 4.5 × 1-mm piece was cut from the wafer, and the ends were lapped and polished to form facets at 45° to the plane of the quantum wells. A cross section of the structure is shown in Figure 5-2. Radiation to be modulated is incident normal to an end facet and is linearly polarized at 45° to the plane of the quantum wells. The radiation makes 10 passes through the MQW structure before exiting through the opposite end facet. This geometry was chosen both to allow a large number of passes through the MQW region and to provide a component of the electric field perpendicular to the plane of the quantum wells, which is the polarization required for intersubband transitions.

The modulator sample was mounted in a variable-temperature cryostat that allowed cooling to ~ 4 K. Previous measurements on this sample showed that the maximum photogenerated intersubband absorption occurs in the temperature range from 45 to 70 K, and hence the present work was conducted at a sample temperature of 55 K. Radiation from a $CO_2$ laser operating at a wavelength of 10.78 $\mu$m was passed through the modulator and then measured by an infrared power meter. Cross-gap radiation was supplied

35

185204-4
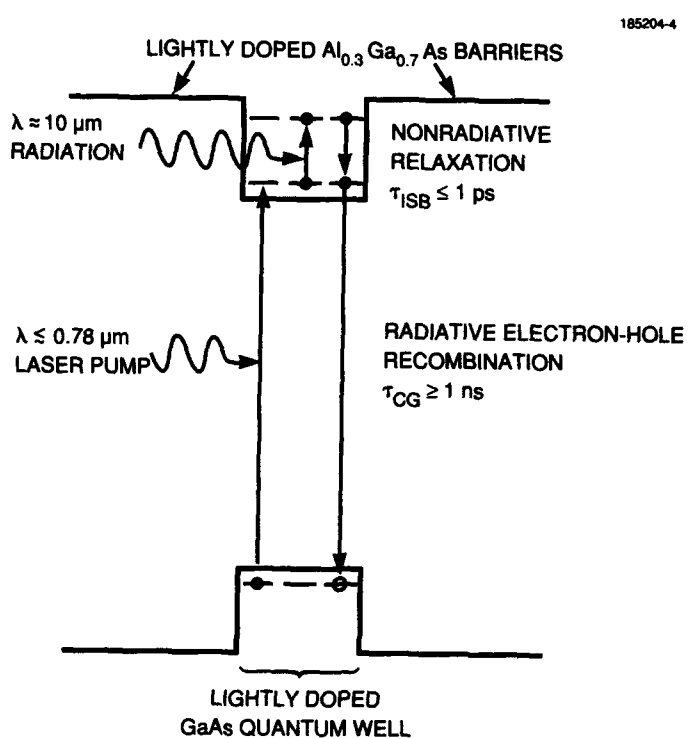
*Figure 5-1. Cross-gap pumping scheme for $CO_2$ laser modulator.*

by either a Ti:$Al_2O_3$ laser or an AlGaAs *p-n* diode laser. Cylindrical lenses were used to illuminate the modulator sample uniformly with cross-gap radiation. The quantity of $CO_2$ laser radiation transmitted through the sample was measured with and without cross-gap illumination. The associated photoinduced change in transmitted power, $\Delta P_T/P_T$, is called the modulation depth.

The measured modulation depth as a function of cross-gap pump power is plotted in Figure 5-3 for different $CO_2$ laser powers. For the lowest $CO_2$ laser power, the modulation depth increases rapidly reaching 80% with only 25 mW of pump power. The modulation efficiency, defined as the power modulated per unit of pump power absorbed, is greatest for such low pump powers. The modulation depth increases much more slowly above 50 mW of pump power, reaching 92% at 200 mW. The measured modulation depth for a given pump power decreases as the $CO_2$ laser power is increased above 0.5 W. For example, with 200 mW of pump power, the modulation depth of a 2.4-W $CO_2$ laser beam is 72%, whereas the modulation depth of a 7-W beam with 250 mW of pump power is 45%. The decrease in modulation depth with $CO_2$ laser power is caused by heating of the modulator sample. With increasing temperature, the mechanism for electron-hole recombination in this sample changes from the relatively slow bound-exciton radiative recombination to the faster free-exciton radiative recombination. The reduction in recombination time causes the density of photogenerated electrons and hence the modulation depth to decrease. The reduced modulation depth for the 2.4- and 7-W power levels is consistent with sample temperatures of 85 to 95 K. Such elevated temperatures can result from absorption of the $CO_2$ laser radiation by background electrons outside the MQW region.

36
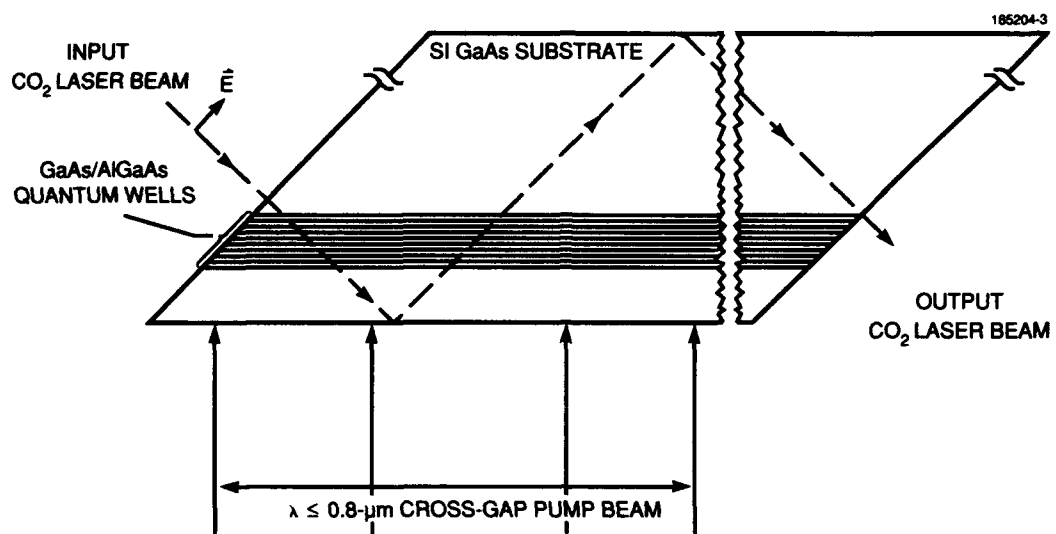
*Figure 5-2. Cross section of modulator structure showing 45° end facets and polarization of the input $CO_2$ laser beam.*
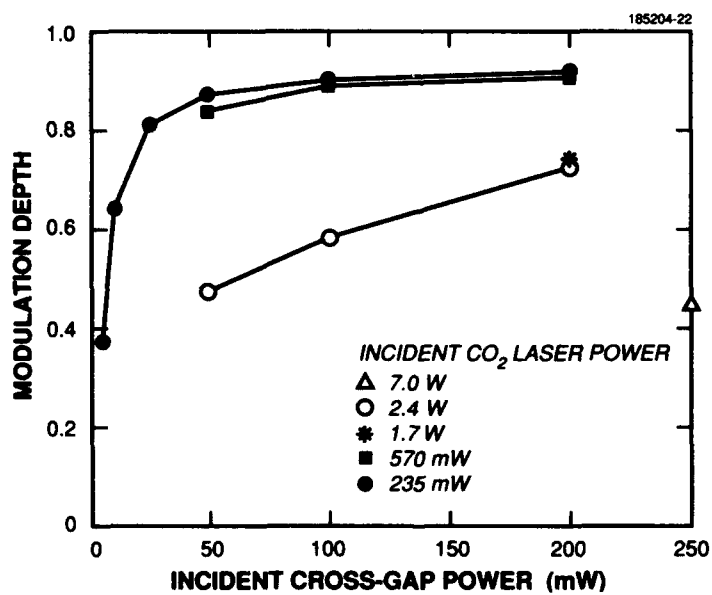


*Figure 5-3. Modulation depth vs cross-gap pump power for several values of $CO_2$ laser power.*

Two properties of this modulator structure that require improvement are the insertion loss and the modulation speed. A 90% insertion loss results from the combined effects of reflection from the end facets, background-carrier intersubband absorption, and frustrated internal reflection. This loss can be reduced somewhat by antireflection coating the end facets and by coating the back side of the substrate with gold. The background intersubband absorption could be reduced by eliminating some of the wells or by reducing the background electron concentration. Either of these solutions would require an increase in pump power to achieve the high modulation depths measured in the present sample. Small-signal measurements of the modulation speed of this device show a 3-dB drop in modulation depth at ~ 5 kHz. This decrease may be caused by a long recombination lifetime for the photogenerated electrons in the quantum wells. Further work is under way to address the speed limitations of the device.

K. A. McIntosh
E. R. Brown
K. B. Nichols

## REFERENCES

1. B. F. Levine, C. G. Bethea, G. Hasnain, J. Walker, and R. J. Malik, *J. Appl. Phys.* **64**, 1591 (1988).

2. J. W. Bales, K. A. McIntosh, T. C. L. G. Sollner, W. D. Goodhue, and E. R. Brown, *Proc. SPIE* **1283**, 74 (1990).

3. R. P. G. Karunasiri, Y. J. Mii, and K. L. Wang, *IEEE Electron Device Lett.* **11**, 227 (1990).

4. M. Olszakier, E. Ehrenfreund, E. Cohen, J. Bajaj, and G. J. Sullivan, *Phys. Rev. Lett.* **62**, 2997 (1989).

# 6. MICROELECTRONICS

## 6.1 CHARGE-TRANSFER INEFFICIENCY IN CCD IMAGERS AT LOW TEMPERATURE

In many scientific and military applications of charge-coupled device (CCD) imagers the device is cooled to suppress dark current. The temperature chosen is usually just sufficient to reduce spatial or temporal dark current noise to negligible levels compared to the noise from other sources. The imagers described below, for example, are typically operated at 230 K (~ −40°C) when used in visible-band space-surveillance applications. Other factors, however, may dictate a lower operating temperature, such as the increased dark current and strong temperature dependence of trapping effects after proton or neutron irradiation. It is therefore important to examine device performance over a broad temperature range. We describe here measurements of charge-transfer inefficiency (CTI) as a function of temperature in buried-channel imagers made on wafers from various sources.

The measurements of CTI were made using a 420 × 420-pixel frame-transfer imager [1]. To measure CTI we uniformly illuminate the device with soft x-rays from the radioisotope $Fe^{55}$, which generates primarily Mn $K\alpha$ x-rays at 5.9 keV. Each x-ray photon generates a highly localized charge cloud of ~ 1620 $e^-$, which is collected by the pixel array and transported to the CCD output. By measuring the amplitude of these charge packets as a function of the number of transfers, one can determine the charge loss per transfer. To ensure that at most only a single photon absorption occurs in any pixel during a frame integration, we use a relatively weak $Fe^{55}$ source (100 $\mu$Ci) located ~ 2 cm away from the device.

Figure 6-1 shows data for a device at 103 K and illustrates the method by which CTI is determined for the output register. For this measurement, only the charge generated in the frame store was used. Each of the 10 traces is a histogram of the signal amplitudes from a region of the frame store comprising 20 columns by 420 rows. In each case a peak can be seen corresponding to the Mn $K\alpha$ x-rays as well as a smaller peak from the less numerous Mn $K\beta$ x-rays at 6.5 keV. The charge packets in each trace have all undergone between 1 and 420 transfers down the frame-store columns, and therefore they all enter the output register with the same distribution of amplitudes. However, the average number of transfers through the output register varies depending on the location of the 20-column region from which the signals originate. In Figure 6-1 the number of such transfers increases from the bottom to top traces, and it is clear that a uniform charge loss occurs along the length of the output register. In this case the register was clocked at 0.5 MHz, and the output-register CTI calculated from the data was 2.9 × 10$^{-4}$. A similar data analysis was used to measure frame-store and imaging-array CTIs. For these calculations, histograms were obtained for regions of 20 rows by 420 columns.

Imagers made on four types of wafers were used in the measurements. Two devices (A and B) were made on $p/p^+$ epitaxial material with a resistivity of ~ 30 $\Omega$ cm and a thickness of 12 $\mu$m, one was made on 1000-$\Omega$ cm bulk material and grown using a magnetic Czochralski (MCZ) method, and one was made on 6500-$\Omega$ cm bulk float-zone silicon. With the exception of device B, the imagers had potential troughs with 3-$\mu$m widths in the output register and 2-$\mu$m widths in the imaging array and frame store [2].
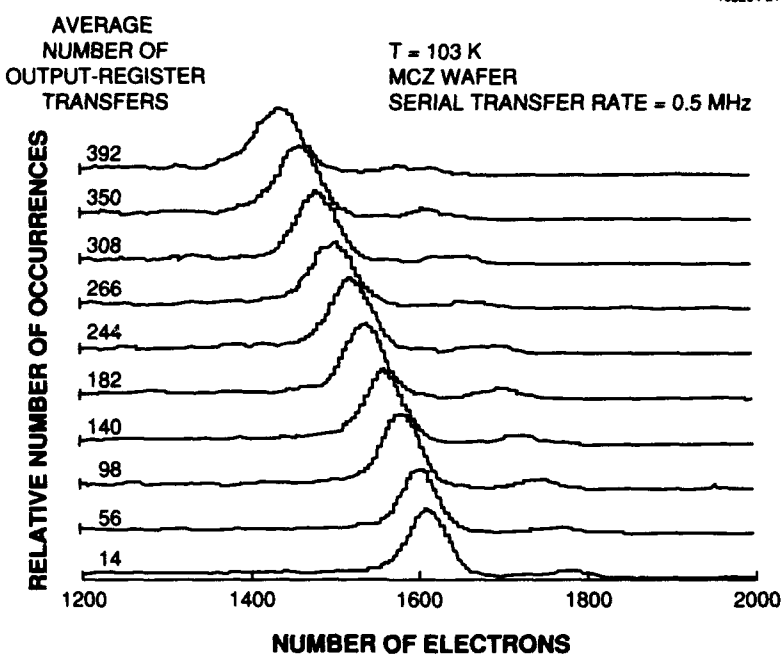
*Figure 6-1. Example of data showing the loss of charge transferred along the output register of a 420 × 420-pixel frame-transfer imager. Each trace is a histogram of charge packets generated by 5.9-keV x-ray photons, each of which generates 1620 e⁻ on average. The histograms are formed from x-ray events at different distances from the CCD output.*

The measured CTI vs temperature for the four devices is shown in Figures 6-2 and 6-3 for the output register and the frame store, respectively. The transfer rate for the frame store is effectively 1.2 kHz and is determined by the time needed to read out each row of 420 pixels at a serial rate of 0.5 MHz before the next frame-store row is advanced into the output register. The data in Figure 6-2 for the output register indicate excellent CTI down to 150 K except for epitaxial device A, in which the CTI deteriorates below 240 K. Below 150 K the three best devices show increased CTI, especially epitaxial device B. However, device B is handicapped by the lack of a narrow trough, which is present in the other devices and provides roughly a tenfold improvement in CTI [2]. Adjusting for this difference, we find that device B is comparable to the bulk devices below 150 K and better above 150 K. Similar conclusions can be drawn from Figure 6-3 showing the corresponding data for the frame store. Good CTI ($< 10^{-4}$) can be maintained down to 120 K in the device grown by the MCZ method and probably also in epitaxial device B if a narrow potential trough is added to the channel.

The finite CTI is the result of bulk trapping effects. Above 150 K it is clear that large variations in trap concentration can occur depending on the wafer source, while below 150 K comparable deterioration of CTI is exhibited by all four devices; the latter is of particular concern with imagers that must operate near 77 K, such as infrared CCDs using silicide detectors. The nature of the trapping centers in these wafers has not yet been established.

B. E. Burke
M. J. Cooper

40
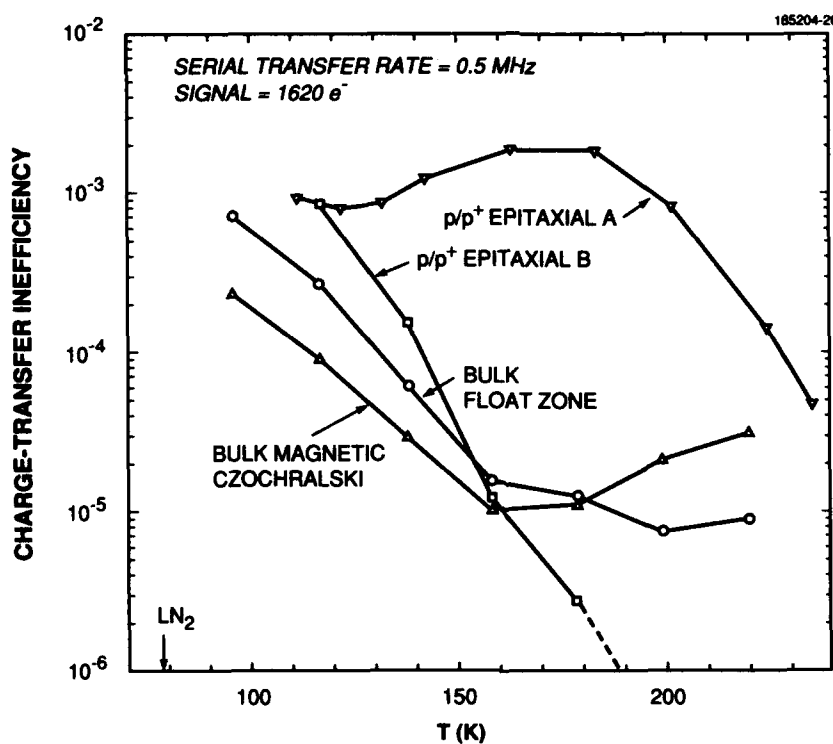
*Figure 6-2. Measured CTI of the output register vs temperature for CCD imagers made on four types of wafers.*
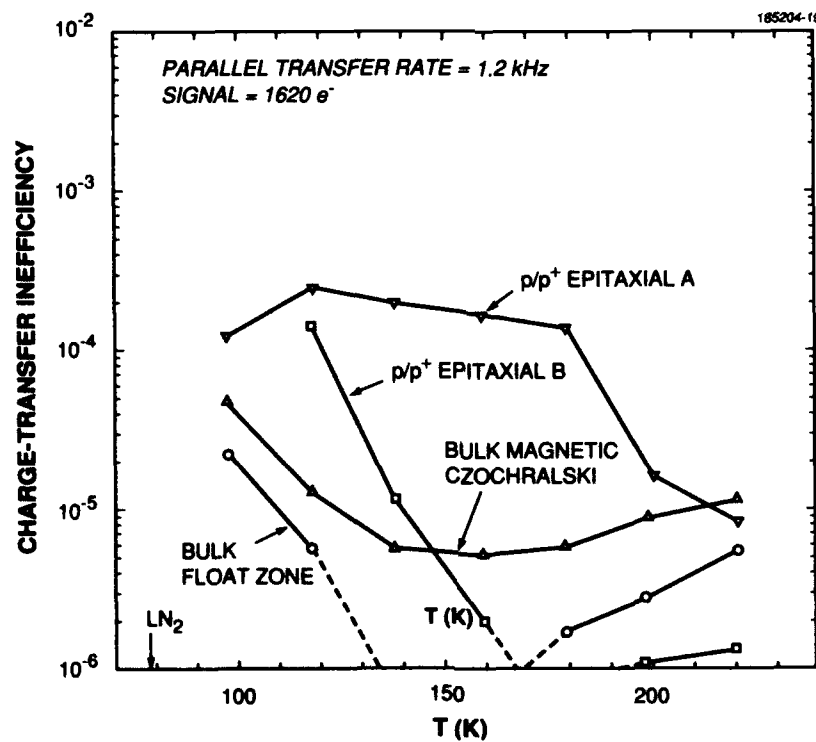


*Figure 6-3. Measured CTI of the frame store vs temperature for the same devices as in Figure 6-2.*

41

# REFERENCES

1. B. E. Burke, R. W. Mountain, D. C. Harrison, M. W. Bautz, J. P. Doty, G. R. Ricker, and P. J. Daniels, *IEEE Trans. Electron Devices* **38**, 1069 (1991).

2. Solid State Research Report, Lincoln Laboratory, MIT, 1990:4, p. 61.

# 7. ANALOG DEVICE TECHNOLOGY

## 7.1 BURIED-CHANNEL CCDs WITH HIGH CHARGE-TRANSFER EFFICIENCY AND LARGE CHARGE CAPACITY FOR LOW TEMPERATURE READOUT OF LONG-WAVELENGTH INFRARED DETECTORS

Monolithic infrared sensors integrating PtSi Schottky-barrier detectors and charge-coupled device (CCD) readout circuitry exhibit excellent performance for thermal imaging in the 3- to 5-$\mu$m spectral region. These sensors are usually cooled to 77 K. Recently developed $Ge_xSi_{1-x}/Si$ heterojunction detectors can extend the wavelength response beyond 10 $\mu$m, but they must be cooled to < 55 K to suppress the dark current. Infrared-CCD focal plane arrays utilizing the new detectors for long-wavelength infrared imaging must therefore incorporate CCDs capable of efficient operation at these low temperatures.

At room temperature the charge-transfer inefficiency (CTI) of buried-channel CCDs can be < $10^{-6}$, but at low temperatures the performance can be severely degraded by trapping of electrons in shallow levels in the buried channel [1]. In general, CTI increases with increasing defect and donor concentration in the buried channel and with decreasing temperature. For operation down to 50 K, the donor concentration can be lowered sufficiently to obtain an acceptable CTI, but this decrease reduces the CCD charge capacity and therefore the dynamic range.

We have designed and fabricated $320 \times 244$-element focal plane arrays with a four-phase interlaced readout configuration of CCDs having a two-step, phosphorus buried channel [2] tailored to allow efficient operation at low temperatures while maintaining large charge capacity. After the first implant, a 16-h anneal at 1140°C is performed to reduce the implantation damage. The second implant is annealed for only 3 h at 1000°C. Simulations predict that the first implant is ~ 4 $\mu$m deep and has a surface concentration of $3 \times 10^{15}$ cm$^{-3}$, while the second implant is ~ 1 $\mu$m deep and has a surface concentration of $3 \times 10^{16}$ cm$^{-3}$.

The predicted channel-doping profiles for imagers with and without the second implant are shown in Figures 7-1(a) and 7-1(b), respectively. Also shown are the calculated electron distributions for different signal levels up to the maximum charge packets allowed by the –4- to +2-V clock swing. The second implant, which is shallow but has a high concentration, moves the channel closer to the surface, as seen in the figures. This results in a higher channel capacitance and more charge per voltage swing. Another effect is to increase the maximum signal that can be confined in the buried channel before the charge reaches the surface. The second implant is carefully selected so that this increase in the charge-handling capacity of the wells does not occur at the expense of increasing the CTI. Simulations show that for a low signal level, where the effect of charge trapping is relatively more important, the electrons are deep in the low-concentration region where there are few traps. For larger signals the electrons spread into the shallow heavily doped region of the buried channel. The simulations predict charge capacities for the double- and single-implant CCDs of $1.2 \times 10^6$ and $2.2 \times 10^5$ electrons, respectively, compared with our experimental values of $1.0 \times 10^6$ and $3.3 \times 10^5$ electrons. In conventional CCDs the channel is shallow (< 1 $\mu$m) and the fields are tightly confined under the gate. These structures are therefore relatively insensitive to two-dimensional effects. In the CCDs just described, on the other hand, both the lateral diffusion of the channel implant and the fringing fields coupling the channel to the field region can have a large influence on the characteristics of the devices. Both effects were considered in our modeling.
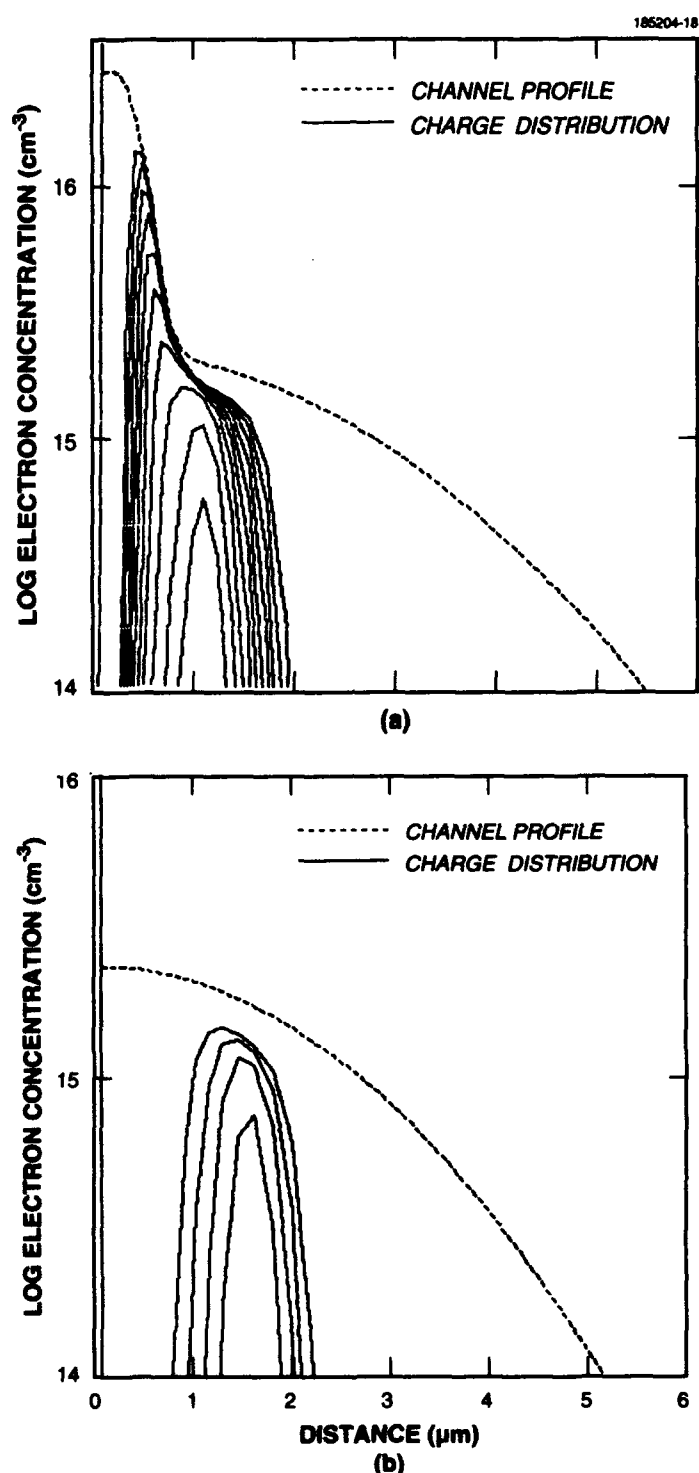
*Figure 7-1. Predicted channel profiles and charge distributions for (a) double-implant and (b) single-implant CCDs.*

44
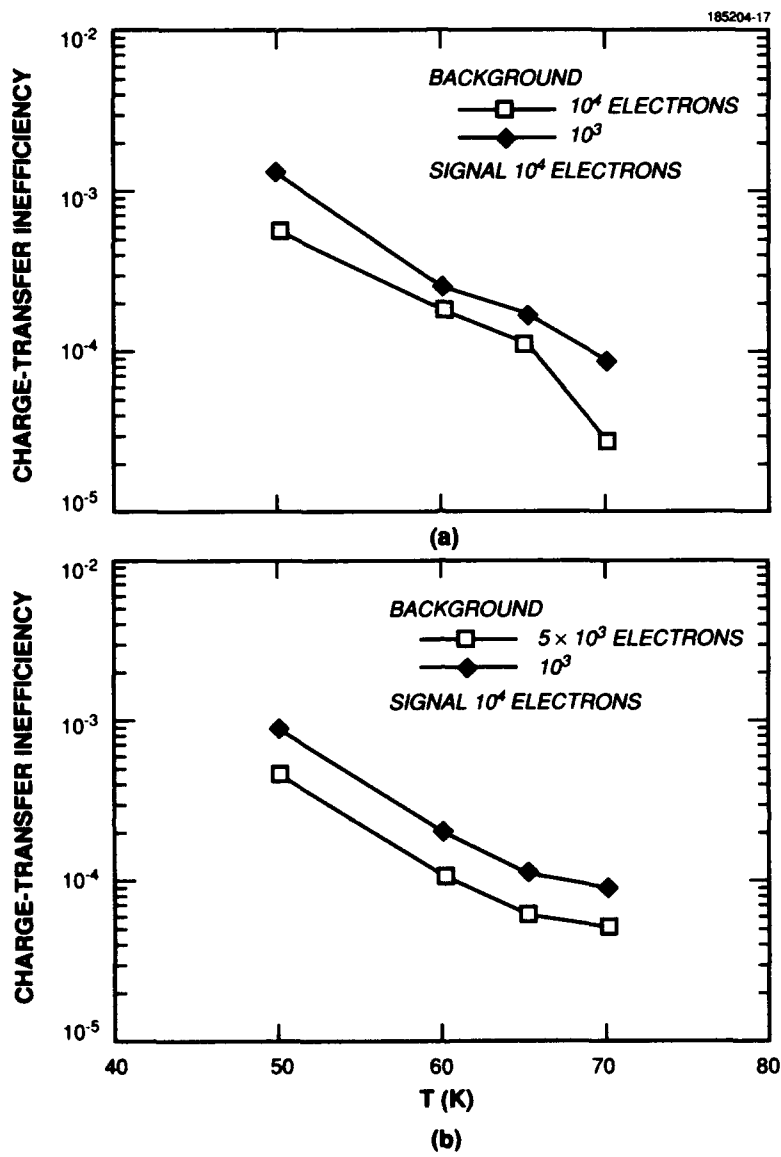
*Figure 7-2. Measured CTI for different temperatures and background levels for (a) double-implant and (b) single-implant CCDs.*

The CTI values measured at different temperatures and background levels for double- and single-implant CCDs are shown in Figures 7-2(a) and 7-2(b), respectively. In all cases the signal charge level is $10^4$ electrons. The CTI of the double-implant CCDs is only slightly higher than that of the single-implant devices. At 77 K, the CTI of the double-implant CCDs is about an order of magnitude lower than that of conventional CCDs [2]; at 50 K, it is $\sim 10^{-3}$, a value that should be adequate for most imaging applications.

A. L. Lattes

B-Y. Tsaur

45

## 7.2 OPERATION OF HIGH-$T_c$ SUPERCONDUCTIVE MATCHED FILTERS AT 77 K

Multigigahertz signal processing has previously been demonstrated using conventional, low-$T_c$ superconductive tapped-delay-line chirp filters [3]. Recently, chirp filters have been demonstrated using thin films of the high-$T_c$ superconductor $YBa_2Cu_3O_{7-x}$ (YBCO) [4]. These high-$T_c$ filters are fabricated using both electron-beam-evaporated, post-annealed YBCO films [5] and in-situ-sputtered YBCO films [6] and operate as designed at temperatures as high as 77 K. The relatively high cryogenic operating temperature opens up many potential field-based-system application areas, such as chirp-transform spectral analysis and matched filtering in radar signal analysis.

Figure 7-3 is a photograph of a matched pair of YBCO chirp filters. The design uses 120-$\mu$m-wide 40-$\Omega$ signal lines in the tapped portion of the device. The taps form backward-wave couplers, and the couplers have a peak response at the frequency for which the coupler is 1/4 wavelength long. By making the length of the couplers inversely proportional to the distance down the line, the filter has a local resonant frequency that is a linear function of the delay (dispersive delay with a quadratically varying phase). These chirp filters contain 48 backward-wave couplers. A Klopfenstein-taper impedance transformer is used to make the transition from narrow (50 $\mu$m wide) 50-$\Omega$ input/output lines to the much wider 40-$\Omega$ lines in the dispersive portion of the device. The impedance transformer aids in the fabrication of the device by reducing the length of 50-$\mu$m-wide transmission line to a small fraction of the total line length. The 120-$\mu$m-wide lines are much more tolerant of defects than 50-$\mu$m-wide lines. Defects can
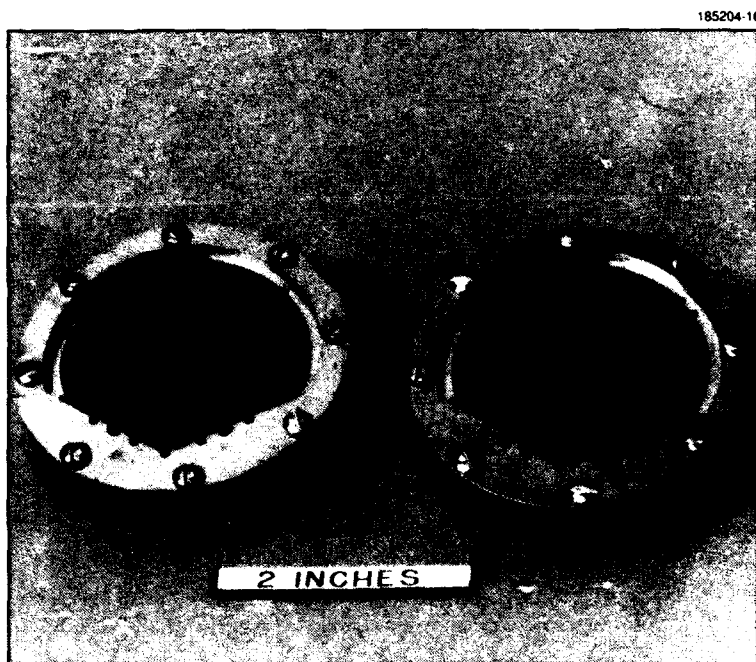


*Figure 7-3. Photograph of high-$T_c$ superconductive matched filter pair. These filters were fabricated on 5-cm-diam $LaAlO_3$ substrates with $YBa_2Cu_3O_{7-x}$ signal lines and silver ground planes. The flat-weighted chirp filter is shown on the left and the Hamming-weighted chirp filter on the right.*

appear in the YBCO film, or can be introduced in the photolithographic patterning process. The fabrication of YBCO chirp filters has been described previously [4]. Silver ground planes are used because YBCO ground planes would not significantly reduce the propagation loss for these linewidths and operating frequencies, similar to the results obtained for resonator-based YBCO microstrip filters [7].

A matched filter pair consists of two chirp filters, each of which generates signals that are time-reversed with respect to the other. A single chirp filter, such as either of those shown in Figure 7-3, can be used to generate both upchirps and downchirps. An upchirp has a positive slope for its frequency-vs-time characteristic, while a downchirp has a negative slope. An upchirp and downchirp represent time-reversed signals if the bandwidths and time delays are the same.

The impulse response is a good measure of the quality of a matched filter pair. One chirp filter (the expander) is used to generate a chirp waveform by passing an impulse through it. The chirp waveform is then passed through the other chirp filter (the compressor) having an impulse response that is the time-reverse of the first filter. The matched output signal energy is compressed coherently into a quasi-impulse, or compressed pulse, with a width that is inversely proportional to the bandwidth of the chirp filters. Because the input to the compressor is the time-reverse of its impulse response, the output is effectively the autocorrelation of the input signal. By varying the weighting of the backward-wave couplers, the sidelobe level of the autocorrelation can be tailored. A Hamming-weighted compressor is used in this YBCO filter pair to substantially reduce the sidelobe level.

The designed and measured transmission responses of a Hamming-weighted YBCO chirp filter with silver ground planes are shown in Figure 7-4 as a function of frequency. The designed response is calculated assuming lossless transmission lines, and agreement with the 77-K measurement is quite good. The deviation from design is due to signal feedthrough in the package and to spurious reflections generated by defects in the filter and particulates that separate the stripline substrates. The response of a flat-weighted YBCO chirp filter operating at 77 K has been measured previously in both the time [8] and frequency [9] domains. Figure 7-5 shows the compressed pulse generated using a flat-weighted YBCO chirp filter as the expander and a Hamming-weighted YBCO chirp filter as the compressor. The compressed pulse response is quite good, although the relative sidelobe level of –23 dB is ~ 9 dB higher than that obtained in previous work with niobium-on-silicon chirp filters operating at 4.2 K [10].

We have demonstrated a matched pair of high-$T_c$ superconductive chirp filters. The matched pair has been used to generate a compressed pulse at 77 K. The chirp filters are fabricated from thin films of YBCO on 5-cm-diam LaAlO$_3$ substrates. The filters have a bandwidth of 2.7 GHz, a dispersive delay of 11 ns, and a total delay of 14 ns, including the tapered-line impedance transformers. The total length of patterned YBCO transmission line for each filter is 0.8 m.

W. G. Lyons            P. M. Mankiewich*

R. S. Withers          M. L. O'Malley*

J. M. Hamm
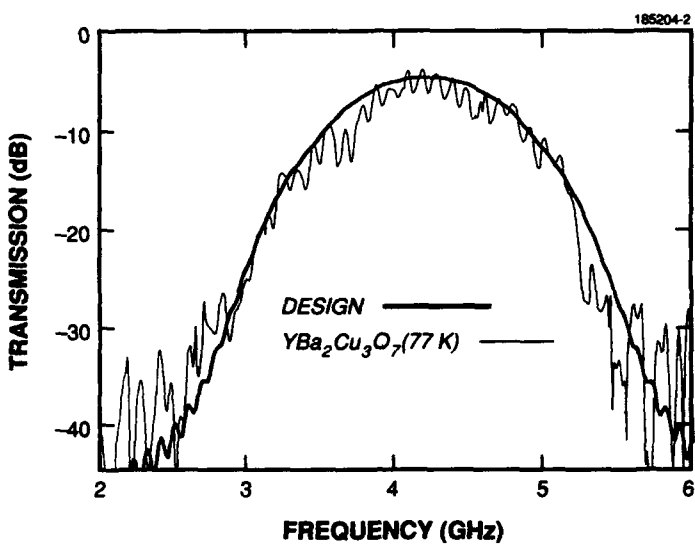
*Figure 7-4. Comparison of the designed and measured transmission responses of the Hamming-weighted high-$T_c$ superconductive chirp filter. The designed response was calculated assuming lossless transmission lines. The design parameters were 5-dB insertion loss, 11-ns dispersive delay, 2.7-GHz bandwidth, and 4.2-GHz center frequency. The measured response was obtained at 77 K.*
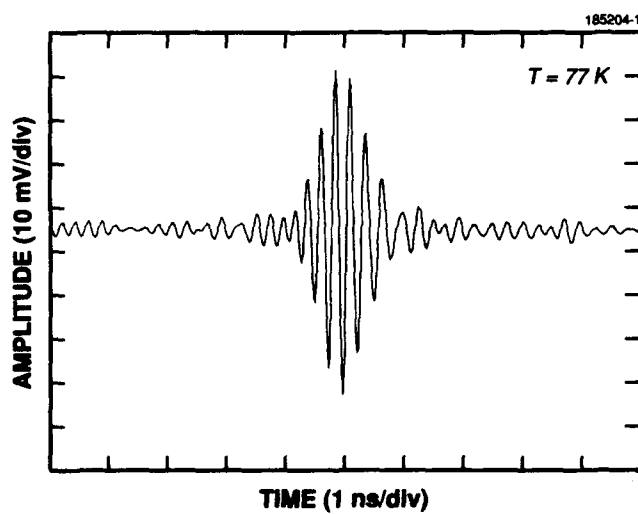


*Figure 7-5. Compressed pulse response of the high-$T_c$ superconductive matched filter pair measured at 77 K. The matched pair consisted of a flat-weighted chirp filter as the expander and a Hamming-weighted chirp filter as the compressor.*

48

# REFERENCES

1. E. K. Banghart, J. P. Lavine, E. A. Trabka, E. T. Nelson, and B. C. Burkey, *IEEE Trans. Electron Devices* **38**, 1162 (1991).

2. T. S. Moss (ed.), *Handbook on Semiconductors*, Vol. 4 of *Device Physics*, C. Hilsum, ed. (Amsterdam, North Holland, 1981), Chap. 3B.

3. R. S. Withers, Alfredo C. Anderson, J. B. Green, and S. A. Reible, *IEEE Trans. Magn.* **MAG-21**, 186 (1985).

4. W. G. Lyons, R. S. Withers, J. M. Hamm, Alfredo C. Anderson, P. M. Mankiewich, M. L. O'Malley, and R. E. Howard, *IEEE Trans. Magn.* **27**, 2932 (1990).

5. P. M. Mankiewich, J. H. Scofield, W. J. Skocpol, R. E. Howard, A. H. Dayem, and E. Good, *Appl. Phys. Lett.* **51**, 1753 (1987).

6. N. Newman, B. F. Cole, S. M. Garrison, K. Char, and R. C. Taber, *IEEE Trans. Magn.* **27**, 1276 (1990).

7. W. G. Lyons, R. R. Bonetti, A. E. Williams, P. M. Mankiewich, M. L. O'Malley, J. M. Hamm, Alfredo C. Anderson, R. S. Withers, A. Meulenberg, and R. E. Howard, *IEEE Trans. Magn.* **27**, 2537 (1990).

8. W. G. Lyons, R. S. Withers, J. M. Hamm, Alfredo C. Anderson, P. M. Mankiewich, M. L. O'Malley, R. E. Howard, R. R. Bonetti, A. E. Williams, and N. Newman, *1991 IEEE MTT-S Int. Microwave Symp. Dig.* (IEEE, New York, 1991), Vol. 3, p. 1227.

9. W. G. Lyons, R. S. Withers, J. M. Hamm, R. H. Mathews, B. J. Clifton, P. M. Mankiewich, M. L. O'Malley, and N. Newman, to be published in *Proc. Picosecond Electronics Optoelectronics Conf.* (Optical Society of America, Washington, D.C., 1991).

10. M. S. DiIorio, R. S. Withers, and Alfredo C. Anderson, *IEEE Trans. Microwave Theory Tech.* **37**, 706 (1989).

# REPORT DOCUMENTATION PAGE

*Form Approved*
*OMB No. 0704-0188*

| 1. AGENCY USE ONLY (*Leave blank*) | 2. REPORT DATE 15 August 1991 | 3. REPORT TYPE AND DATES COVERED Quarterly Technical Report, 1 May – 31 July 1991 |
|---|---|---|

**4. TITLE AND SUBTITLE**

Solid State Research

**6. AUTHOR(S)**

Alan L. McWhorter

**5. FUNDING NUMBERS**

C — F19628-90-C-0002
PE — 63250F
PR — 221

**7. PERFORMING ORGANIZATION NAME(S) AND ADDRESS(ES)**

Lincoln Laboratory, MIT
P.O. Box 73
Lexington, MA 02173-9108

**8. PERFORMING ORGANIZATION REPORT NUMBER**

1991:3

**9. SPONSORING/MONITORING AGENCY NAME(S) AND ADDRESS(ES)**

Air Force Systems Command, USAF
Andrews AFB
Washington, DC 20334-5000

**10. SPONSORING/MONITORING AGENCY REPORT NUMBER**

**11. SUPPLEMENTARY NOTES**

**12a. DISTRIBUTION/AVAILABILITY STATEMENT**

Approved for public release; distribution is unlimited.

**12b. DISTRIBUTION CODE**

**13. ABSTRACT (*Maximum 200 words*)**

This report covers in detail the research work of the Solid State Division at Lincoln Laboratory for the period 1 May through 31 July 1991. The topics covered are Electrooptical Devices, Quantum Electronics, Materials Research, Submicrometer Technology, High Speed Electronics, Microelectronics, and Analog Device Technology. Funding is provided primarily by the Air Force, with additional support provided by the Army, DARPA, Navy, SDIO, NASA, and DOE.

**14. SUBJECT TERMS**

| | | | |
|---|---|---|---|
| electrooptical devices | high speed electronics | optical interferometers | diamond cold cathodes |
| quantum electronics | microelectronics | nonlinear optics | charge-coupled devices |
| materials research | analog device technology | laser modulation | superconductive filters |
| submicrometer technology | lasers | ultraviolet lithography | |

**15. NUMBER OF PAGES**
78

**16. PRICE CODE**

| 17. SECURITY CLASSIFICATION OF REPORT | 18. SECURITY CLASSIFICATION OF THIS PAGE | 19. SECURITY CLASSIFICATION OF ABSTRACT | 20. LIMITATION OF ABSTRACT |
|---|---|---|---|
| Unclassified | | SAR | SAR |